GENERATION OF THE SITE-ADAPTED CLEAREST-SKY YEAR OF DIRECT NORMAL IRRADIANCE FOR SOLAR CONCENTRATING TECHNOLOGIES

Alberto Royo[a*], Ignacio García[a], José Luis Torres[a]

[a] Department of Projects and Rural Engineering, Public University of Navarre, Los Olivos Building, Campus Arrosadía, 31006 Pamplona, Spain.

[*] Corresponding author: Tel.: +34 948 168405, Fax: +34 948 169148, email: alberto.royo@unavarra.es

ABSTRACT

Concentrating photovoltaic and thermoelectric solar facilities base their operation on collecting the direct component of solar radiation. Given that the direct beam that reaches the Earth's surface varies greatly in time and space, it is common to assist the bankability of projects with a solar resource assessment. Sun-tracking collector plants are typically examined via a time series analysis of measured weather data and test reference years. Such analysis, which considers the eventual presence of clouds, may be complemented with the use of the synthetic clear-sky year assuring the maximum theoretical availability of direct normal irradiance at a site. This work introduces for the first time the concept of site-adapted clearest-sky year (CSY) and provides a methodology for its generation. Three methods to build the CSY and one algorithm to detect clear-sky moments are proposed.

KEY WORDS

Direct normal irradiance, clear-sky year, concentrating photovoltaics, concentrating solar power, solar resource assessment.

Nomenclature			
BIFMCP	Backwards Interpolate Forward Measure Correlate Predict	IMCP	Interpolate Model Measure Correlate Predict
CPV	Concentrating photovoltaics	m	Air mass
CSY	Site-adapted clearest-sky year	MCP	Measure Correlate Predict
CSY_{BIFMCP}	CSY obtained with BIFMCP	MCPI	Measure Correlate Predict Interpolate
CSY_{IMCP}	CSY obtained with IMCP	TL(AM2)	Linke turbidity factor for air mass 2
CSY_{MCPI}	CSY obtained with MCPI	TMY	Typical meteorological year
DHI	Diffuse horizontal irradiance, W/m^2	UMY	Untypical meteorological year
DNI	Direct normal irradiance, W/m^2	XMY	Extreme meteorological year
DNI_r	DNI in the reference site, W/m^2		**Greek symbols**
DNI_t	DNI in the target site, W/m^2	α	Slope of the regression line
GCR	Ground cover ratio	β	Offset of the regression line
GHI	Global horizontal irradiance, W/m^2	$\delta_{Rayleigh}$	Integrated Rayleigh optical thickness for a clean and dry atmosphere
G_{SC}	Solar constant (1367 W/m2)	E	Correction due to Sun-Earth distance

1. INTRODUCTION

A solar energy facility project should rely on an accurate assessment of the local solar resource. This examination would supply any subsequent simulation with essential local radiation knowledge, enabling a comprehensive evaluation of the facility performance subjected to different working hypotheses.

Considering that the direct normal irradiance (DNI) is the energy source for concentrating plants, when it comes to assessing their electrical long-term output, it would be convenient to have long time series of DNI measurements registered at very high frequency (on the order of a few minutes) at the project site. Unfortunately, such data are not generally available and it is necessary to resort to the use of mathematical models to estimate the local DNI.

For engineering applications, the literature reports numerous clear sky models that determine the DNI from the knowledge of atmospheric attenuators, both spectral (SMARTS2, described in [1, 2]) and parametric or broadband (Bird and Hulstrom, ESRA, Solis, or REST2 [3-6]). Far fewer models address the problem in the case of skies with clouds. One of them is METSTAT (Meteorological/Statistical) [7], a parametric model suitable for any type of sky which has been successfully used in the United States to generate the National Solar Radiation Database (NSRDB) [8]. However, METSTAT is difficult to apply outside the United States due to the general lack of cloud coverage data. A more recent parametric model, with the same capability as METSTAT, is the MRM (Meteorological Radiation Model) [9, 10], developed in the National Observatory of Athens (NOA). MRM can work worldwide and uses meteorological data (temperature, relative humidity, atmospheric pressure, sunshine duration), actual atmospheric aerosol data, aerosol model, ozone amount and cloud products (cloud optical depth and cloud fraction) as input.

In contrast to those physical models for engineering applications, which compute the DNI after considering the atmosphere as an attenuating medium in the path of the extraterrestrial radiation towards the Earth's surface, global-to-direct models estimate the DNI from global horizontal irradiance (GHI) data as the main input. This is the case for the DISC [11], DirInt [12] or DirIndex [13] models, which are valid for any type of sky. Global-to-direct models benefit from the greater availability of global radiation data measured on the ground.

Another alternative to obtain the DNI for any type of sky are highly sophisticated spectral codes (LOWTRAN [14], MODTRAN [15], libRadtran [16]). These models are typically used by atmospheric scientists to carefully analyze the behavior of the atmosphere or to evaluate climate change, and can incorporate cloudiness and its distribution into different layers. In engineering applications, this high degree of detailed information to the model may be relaxed depending on the required accuracy of the results.

Figure 1 summarizes the models to determine the local DNI. Depending on the type of sky and available input variables, the project designer will have to choose the model to determine the locally incident DNI. Table 1 in Gueymard [17] contains an interesting list of clear-sky parametric models that currently may be enlarged with Solis, ESRA, REST2 and McClear [18] models. McClear is a physical model for cloud-free skies, which is based on look-up tables computed with libRadtran.

FIGURE 1

Fig. 1. Set of models to determine the local DNI for the cases of clear sky and any sky.

The input parameters to the models can be obtained from on-ground instruments or from satellite on-board instruments. Instrumentation installed on the surface of the Earth offers very accurate measurements of radiation components, such as DNI, or of atmospheric variables (aerosol levels, water vapor, ozone, barometric pressure, temperature…) that feed the models to deliver the DNI. Satellite data sources are often employed when there are no data available from on-ground instruments. Satellites can provide an estimation of DNI for large regions of the Earth, at the cost of a lower accuracy compared to conventional on-ground instrumentation. To that end, the terrestrial albedo derived from the radiance measured by satellites is used to infer the cloud cover, which, in turn, leads to the global irradiance on horizontal surface under any sky. For clear skies, a model like the one involved in the production of the European Solar Radiation Atlas (ESRA) [4, 19] can be applied to estimate GHI. Then, with the GHI or with satellite measurements of atmospheric variables, and one of the models in Figure 1, the DNI can be determined. Examples of satellite data sources are, among others, the TOMS [20] and Terra [21] missions of the United States, or the CM SAF project [22] of the European Union.

In addition to the models and data sources accessible for free, commercial solar radiation databases exist, such as Meteonorm [23], Solar Radiation Data (SoDa) [24], and others. These products offer DNI values for a specific location for customers who do not want to manage terrestrial and satellite measurements, interpolations, and any of the models discussed because the commercial products perform this service.

Bearing in mind about the modeling tools and data sources of the foregoing paragraphs, today it is possible to claim that acquisition of DNI data is no longer an insurmountable obstacle for solar resource assessment. Rather, it may be said that the pillars for a good assessment are the quality of the DNI data used, and the suitability of the chosen model for the project site. The latter may be decided from a benchmark of models, but after all this also relies on the quality of the DNI data. Therefore, the quality of the DNI data becomes the key for a trustworthy assessment.

Closely linked to the quality of data, features such as the representativeness of the gathered data and their interannual variability are crucial in evaluating the feasibility of a project. These issues have been traditionally dealt with typical meteorological years (TMY).

A typical meteorological year, also known as test reference year, is a synthetic year ordinarily composed of the concatenation of 12 actual months, usually from different years, drawn from the historical series of measurements of several meteorological indicators. In particular, once the long DNI series for a project site is known, it can be incorporated into the construction of a TMY for that location.

The use of TMYs has been proposed in many papers (Hall et al., Festa and Ratto, Gazela and Mathioulakis, Thevenard and Brunger, Wilcox and Marion, García and Torres [25-30]), and included in standards (EN ISO 15927-4, 2005) [31], when, in the design phase, it is desired to ascertain the long-term performance of solar energy harnessing facilities.

By definition TMYs reproduce well the typical conditions, but miss extreme values. For applications where extremes matter, it is advisable to build an extreme year. In the field of bioclimatic architecture and building energy performance, some solutions for this topic have been proposed. While Narowski et al. [32] have developed several untypical meteorological years (UMY) by varying the weighting indices implicated in the generation of TMYs, Crawley and Lawrie [33] have created extreme meteorological years (XMY) by selecting months with daily maxima and minima, and highest and lowest hourly average values of the set of variables involved in the TMYs.

Inspired by extreme years and as a complement to TMYs, a site-adapted clear-sky year of maximum energy content might provide overlooked opportunities to enrich the analysis and understanding of the concentrating technology plants. In the framework of DNI, a clear-sky year is an entire year of a permanently clear or cloud-free line-of-sight between the solar disc and a Sun-pointing device placed at the location of interest. Consequently, the site-adapted clear-sky year with maximum energy content will be the clear-sky year made of the clear-sky days with the highest energy content for a given location. Since "site-adapted clear-sky year with maximum energy content" is a little bit long for a name, hereafter it will be referred to as "site-adapted clearest-sky year", and even simpler, "clearest-sky year" (CSY). The term "clearest" implies the absence of clouds and the reduced presence of aerosol.

Apart from semantic questions, the important thing is that the clearest-sky year is site-specific and constitutes the scenario of maximum theoretical available solar resource, which at the same time is the most critical context for capture losses in that location. In the case of a Sun-tracking collector facility the CSY might be at least helpful to better characterize the performance, test different plant layouts, and consider the impact of potential restrictions on the range of motion of the trackers. The amount of DNI on the trackers, assuming no restrictions on their motions, depends on the mutual shadowing and the type of sky. Shadows can be considered deterministically by solving a geometrical problem. However, the type of sky introduces uncertainty due to the partial degrees of cloudiness. The site-adapted CSY, as with any clear-sky year, removes cloudiness from the calculations and, additionally, sets the upper limit of radiation for a site. The same reasoning, when restricting the range of motion of the Sun trackers, is valid and now viable because the causes and effects under CSY are perfectly identified. As an example of application of the CSY, Figure 2.a represents the pattern layout of a plant of two-axis solar trackers with squared CPV planes, placed at Solar Village (24.907ºN, 46.397ºE). Mutual shadowing, as reproduced in Figure 2.b, will affect the squared CPV planes to a greater or lesser extent.

FIGURE 2

Fig. 2. (a) Pattern layout of a plant of two-axis solar trackers with squared CPV planes, placed at Solar Village (24.907ºN, 46.397ºE). The length and width of any tracker is W, and trackers are equally spaced according to a North-South separation and an East-West separation. (b) A moment of mutual shadowing.

Some results of this example are shown in Figures 3.a and 3.b. Figure 3.a exhibits the annual irradiation contour lines under CSY on a squared CPV plane with no restriction in its two-axis solar tracking. Depending on the North-South separation and the East-West separation between adjacent trackers, which are expressed in number of CPV plane widths, the annual maximum theoretical amount in MJm^{-2} (including shadowing losses) is displayed. From these maxima, Figure 3.b shows the annual irradiation ratio for the same squared CPV plane when restrictions in the zenithal range swept by trackers take place, as a function of the ground cover ratio (GCR) [34], which can be calculated from the North-South and East-West separations. These two graphs reveal that for irradiation the East-West separation is more critical than the North-South one (see Figure 3.a) due to the increment of mutual shadowing. If trackers sweep less zenithal range, the mutual shadowing becomes weaker, although gains achieved by reducing the shadows are more than lost by limiting the tilting of the trackers (see Figure 3.b). Since the number of hours of high Sun varies with latitude, the zenithal range of trackers will also affect differently and, therefore, the spacing between curves in Figure 3.b will vary with latitude too. Through the use of a CSY all these issues can be rigorously quantified and other interesting enquiries can be conducted. For instance, the influence of several factors on irradiation like the type of sky, the GCR, the latitude, restrictions in motions, or the shape of the CPV plane, not only for Solar Village but also for other sites. These intra-site and inter-site comparisons provide insight into projects and help improve bankability.

FIGURE 3

Fig. 3. (a). Annual irradiation contour lines (shadowing losses included) under CSY on a squared CPV plane with no restrictions in its two-axis solar tracking. (b) Annual irradiation ratio for the same squared CPV plane submitted to restrictions in the zenithal range.

The aim of this contribution is to introduce the concept of CSY for direct normal irradiance, mainly intended for concentrating photovoltaic and concentrating solar power applications and their energy calculations, and to describe the methodology for the generation of such a year.

2. METHODOLOGY AND DATA

2.1. Description of the site-adapted CSY

Below are some remarks on the nature and requirements of the CSY for the direct normal irradiance:

- A CSY is composed of only clear-sky DNI values. This obliges combining the measured DNI data and the modeled DNI data in the same CSY series.
- In line with Hirsch et al. [35], the time step between adjacent data points should be close to 1 minute to support high accuracy in the subsequent system simulations. In this work, 1-minute DNI series have been developed.
- Every day of a CSY must be of maximum energy content to later procure the realistic maximum annual radiation. Since clear sky, in the sense defined in the introduction, is a prerequisite, the aerosol load will determine the level of DNI at each moment. Therefore, the cleaner the atmosphere, the higher the DNI levels are on the surface. To select the CSY dates, days with a maximum energy content are first assembled into a clear-sky DNI series that should be as long as possible of measured and modeled data. Then, 365 groups are made with days sharing the same ordinal day number. The CSY is built with the most energetic dates in each of those groups.
- A CSY must be a complete year with no data gaps. Therefore, every minute must have a clear-sky DNI value because every minute counts when it comes to calculate the annual radiation.
- To the extent possible, a CSY must be site-adapted because every place has unique sky conditions.
- A CSY must be long-lasting because it is intended to be used as a reference. To fulfill this requirement, the clear-sky DNI series of measured and modeled data should come from as many years as possible.

In the real world it is improbable, though physically possible, that a CSY be observed in its entire extension in the same natural year.

The energy content for a certain day is given by the area enclosed under the DNI. In this work that area has been obtained by integration of the 1-minute DNI values.

2.2. Management of the information stored in several data sets

One of the main purposes of evaluating the solar energy potential at a site is to obtain highly reliable, local, long-term solar resource estimates. Taken to the extreme, this aspiration would need long and expensive on-site measurement campaigns. However, Thuman et al. [36] have shown that the best strategy is to measure the DNI on site for a short period of at least one full year to acquire the usual seasonal variation, and complete the study with data sets spanning much longer periods, ideally coming from reference stations placed in the immediate vicinity of the project site. If there are not any such sites, it is common to utilize satellite-modeled data. According to Schnitzer et al. [37], multiple data sources adequately treated reduce the uncertainty in the solar resource estimates.

A methodology that exploits the information stored in data sets from several data sources is the Measure Correlate Predict (MCP) [36], which is a family of methods extensively employed in the field of wind energy. The MCP methods attempt to reproduce the resource conditions at a project site or target site. This may include filling in missing data and extending the measurements series with predicted DNI values. For this, as stated above, it is necessary to have a short series of DNI measurements at the target site, and a long series of DNI measurements from a geographically proximate reference site. The period of the target site with available data must be covered concurrently by a long series of data from the reference site. This long series must also provide measured reference data for the period with missing target data. Assuming a strong correlation between the reference and target sites, a statistical relation can be derived from the concurrent data sets, mapping the reference data into the predicted data for the target site.

This work uses MCP to lengthen the DNI series and fill gaps at the target site, and linear regression as correlation technique between the concurrent target and reference data:

$$DNI_t = DNI_r \cdot a + b \qquad (1)$$

where DNI_t is the predicted DNI at the target site, DNI_r is the measured DNI at the reference site, and the parameters *a* and *b*, determined by least squares, are the slope and offset of the linear best fit, respectively. The procedure of correlating the reference and target sites to localize the reference data in the target site is known as site adaptation [38].

2.3. Methodology of generating the site adapted CSY

The circumstances around the problem of generating the CSY are illustrated in Fig. 4. The core of the figure (labeled as (h), background filled in blue) shows the MCP method feeding the short and the long DNI series (labeled as (f) and (g), respectively), to supply a long clear-sky DNI series adapted to the site or target (labeled as (i)). The short DNI series (f) has most likely been acquired in an on-site monitoring campaign, taking only the measurements corresponding to clear-sky moments, whereas the long DNI series (g) is to be built from measurements of DNI and/or atmospheric parameters from nearby stations or satellite observations under clear-sky conditions. To fill gaps in data series and to compose the long reference DNI series (g), some data manipulations should be carried out at the pre-MCP stage. Analogously, there exists a post-MCP stage to compile the site-adapted CSY (labeled as (m)) from the long clear-sky DNI series adapted to the site (i) produced in the MCP core (h).

FIGURE 4

Fig. 4. Methodology to generate a site-adapted CSY.

Several data transformations can be performed in the pre-MCP stage. It is possible to jump from the atmospheric parameter domain to the DNI domain with small errors [39] if accurate atmospheric parameters have been registered, utilizing a rigorous implementation of the transmittances in the chosen solar radiation model. Similarly, it is possible to jump backwards from the DNI domain to the atmospheric parameter domain through accurate DNI measurements and a sufficient solar radiation model [40, 41]. The isosceles trapezium, labeled as (a) and plotted with the dashed line, represents the complexity of gathering high quality clear-sky atmospheric parameters, which could be the starting point to obtain the DNI series. Three paths have been sketched that link the atmospheric parameter domain to the DNI domain. The first path, solid line, consists of linearly interpolating (labeled as (b)) the clear-sky atmospheric parameters to fill gaps, and then applies a suitable solar radiation model (labeled as (c)) to obtain the corresponding clear-sky DNI value for a certain input of atmospheric parameters. The linear interpolation (b) of the clear-sky atmospheric parameters can be assumed as valid under clear and stable atmospheric conditions, and relatively uniform aerosol load over short intervals, which is the normal behavior of aerosols. The second and third paths, dotted lines, consist of applying a solar radiation model (labeled as (d)) to acquire the corresponding clear sky DNI values, and vice versa, by applying backwards the solar radiation model (labeled as (e)) to obtain the input of the atmospheric parameters. These second and third paths maintain the data gaps that will later have to be filled.

For the paths drawn in the dotted line (labels (d) and (e)) in the pre-MCP stage, the ESRA solar radiation model has been chosen for both transformations because it reduces to one parameter, the Linke turbidity factor [42] for an air mass equal to 2. The effects of the atmospheric turbidity and, therefore, the attenuation of clear-sky DNI are given by Eq. (2), which shows the ESRA formula to determine DNI. Eq. (3), deduced from Eq. (2), is the analytical expression to determine the Linke turbidity factor for an air mass of 2:

$$DNI = G_{SC} \cdot \varepsilon \cdot e^{(-0.8662 \cdot TL(AM2) \cdot m \cdot \delta_{Rayleigh})} \tag{2}$$

$$TL(AM2) = -\frac{L_n\left(\frac{DNI}{G_{SC} \cdot \varepsilon}\right)}{0.8662 \cdot m \cdot \delta_{Rayleigh}} \tag{3}$$

where G_{SC} is the solar constant, ε is the correction due to actual Sun-Earth distance, *TL(AM2)* is the Linke turbidity factor for an air mass equal to 2, m is the relative optical air mass, and $\delta_{Rayleigh}$ is the integrated Rayleigh optical thickness for a clean and dry atmosphere.

After the MCP stage, a long clear-sky DNI series adapted to the site (i) and spanning several years is generated. Depending on the path followed in the pre-MCP stage, the series may or may not contain missing data. Therefore, in the post-MCP stage, two possible routes or paths could be taken. The path in the solid line (labeled as (j)), which can be considered as the prolongation of the solid line path from the pre-MCP stage, does not fill data gaps because this task was accomplished in the pre-MCP stage. In parallel to this route, the path in the dotted line (labeled as (k) and (l)) fills the missing data when the output of the MCP has gaps. Both post-MCP routes complete the DNI series for the CSY. Based on this discussion, each day can be characterized in terms of the total energy by its daily sum of 1-minute DNI values (labels (j) and (l)). Then, each of the 365 days of the CSY (m) will be the specific day with the greatest total energy among all days sharing the ordinal day number (1 to 365) throughout the different years present in the output (i) of the MCP process. For instance, if 20 February (ordinal 51) is the day for which its best performing clear-sky day is searched, the day with the greatest total energy will be chosen among all the years with measurements on 20 February.

So far nothing has been said about the detection of clear-sky moments, despite its critical importance. A number of clear-sky detection algorithms can be found in the literature. Some of them, like Long and Ackerman [43], detect moments with completely cloud-free sky vault, and some others, like Smirnov et al. [44], or Polo et al. [45], detect moments with a clear line-of-sight between the solar disc and the site. The former algorithms are too restrictive for concentrating technologies and remove many clear line-of-sight moments. For this reason, the algorithm used to test the McClear solar radiation model, by Lefèvre et al. [18], is suggested to pick the clear line-of-sight moments from an all-sky GHI series.

2.4. Data

What remains in this document is a worked example to illustrate the CSY methodology, with data from the site of Solar Village (24.907ºN, 46.397ºE, 764 meters above sea level, Saudi Arabia). For this location, around four years (1999 to 2002) of 1-minute DNI data have been downloaded from BSRN (Baseline Surface Radiation Network) [46], whereas roughly fifteen years (1999 to 2013) of records of atmospheric variables have been procured from AERONET (Aerosol Robotic Network) [47]. AERONET data are level 2.0, meaning that observations are cloud-screened and quality-assured. As occurs in nature, the DNI measurements of BSRN [48] include overcast and partly-cloudy sky moments together with clear-sky ones, which unfortunately are not identified. The daily information about the ozone has been taken from the TOMS and OMI satellite on-board instruments. The algorithm of Blanco-Muriel et al. [49] is used to determine the position of the Sun.

The MCP requires a short-site series and a long-reference series of DNI measurements. Instead of performing the MCP with the series belonging to different locations, this example uses the short-site series provided by BSRN, which acts as the target site, while the long-reference series comes of AERONET, which acts as the reference site. Normally for the MCP, data from at least another place are needed, or, failing that, from satellites. Since this would only make the example unnecessarily denser, Solar Village has been chosen as an environment with the sole intention of illustrating the model and validating the methodology. Approximately 90% of the DNI measurements are from active cavity radiometer, and 10% from pyrheliometer (see [48]).

Since we have selected AERONET data flagged by AERONET as occurring during clear line-of-sight moments, the corresponding BSRN moments are found by matching the timestamp. The algorithm by Lefevre et al. [18] could have been applied, but the AERONET algorithm has been preferred because it provides ready-to-use information and detects better clear-sky moments with low Sun (but, on the other hand, it promotes the emergence of 15-minute data gaps; see section 3).

2.5. Procedures to create the site-adapted CSY

Consistent with Figure 4, three CSYs have been synthesized using three different procedures. These three procedures, which compute the daily sum of DNI to find the day of maximum energy content for each ordinal day number of the CSY, are:

1. Procedure IMCP (Interpolate, Model, Measure, Correlate, Predict): if at the reference site the atmospheric variables of the clear-sky moments needed to feed the SMARTS2 (selected from a serious benchmark of models for Solar Village, as performed by the authors, whose results are not included in this work) are known, the missing values of the atmospheric variables can be filled using linear interpolation. In early mornings and late afternoons, the atmospheric variables keep the values registered in the first clear-sky moment of the day, and the last

clear-sky moment of the day, respectively. In this way, a complete long series of atmospheric variables at the reference site is achieved. Then, using SMARTS2, this series is transformed into the corresponding long series of DNI values. This strategy of linear interpolation followed by SMARTS2 is represented in Fig. 5. After executing SMARTS2 (and not shown in Fig. 5), the procedure continues with the application of MCP on the long-reference series and on the short-site DNI series to obtain a long clear-sky series adapted to the site.

FIGURE 5

Fig. 5. Strategy of IMCP based on applying linear interpolation to atmospheric parameters, followed by the use of SMARTS2. The short lines in blue are the atmospheric parameter values kept in early mornings and late afternoons.

2. Procedure BIFMCP (Backwards, Interpolate, Forward, Measure, Correlate, Predict): when the clear-sky DNI series at the reference site is known, the ESRA model is applied backwards with Eq. (3) to acquire the TL(AM2) related to those DNI values. Now, the missing TL(AM2) can be filled using linear interpolation. For early mornings and late afternoons, the TL(AM2) values of the first clear-sky moment of the day and of the last clear-sky moment of the day are kept when filling the missing information. When doing this, a long complete series of TL(AM2) values at the reference site is attained. Then, by forward applying the ESRA model with Eq. (2), this series is converted into its corresponding long series of DNI values. This strategy of applying ESRA backwards, followed by linear interpolation, and applying ESRA forwards is represented in Fig. 6. After executing ESRA forwards (and not shown in Fig. 6), the procedure continues with the application of MCP on the long-reference DNI series and the short-site DNI series to obtain a long clear-sky series adapted to the site.

FIGURE 6

Fig. 6. Strategy of BIFMCP based on applying ESRA backwards, followed by linear interpolation of TL(AM2), and applying ESRA forwards. The short lines in blue are the TL(AM2) values kept in early mornings and late afternoons.

3. Procedure MCPI (Measure, Correlate, Predict, Interpolate): instead of interpolating in the pre-MCP stage, if the clear-sky DNI measurements or clear-sky atmospheric variables (SMARTS2 translates them into DNI values) are available, at a high enough frequency, the MCP process can be carried out directly with the series as they are (with missing data). At the output of the MCP process, the clear-sky series adapted to the site must be filled with a linear interpolation. This strategy of applying linear interpolation on the long clear-sky DNI series adapted to the site obtained from the MCP process is shown in Fig. 7.

FIGURE 7

Fig. 7. Strategy of MCPI based on linear interpolation of the DNI data adapted to the site (obtained after application of MCP).

In a sense, it does not matter which procedure or path is followed; what all these paths try to do is to reconstruct, when possible, the day that would have been real if clouds had not been present. If the reference series is long enough, there will be reconstructed days for each ordinal day number, and then the days with the greatest energy content will be determined using the criterion of the maximum daily sum of DNIs.

3. RESULTS AND DISCUSSION

Figures 8, 9 and 10 describe step-by-step the procedures identified as CSY_{IMCP}, CSY_{BIFMCP} and CSY_{MCPI} to obtain the CSY.

FIGURE 8

Fig. 8. Procedure IMCP (Interpolate, Model, Measure, Correlate, Predict) to obtain the site-adapted clearest-sky year CSY_{IMCP} for Solar Village.

FIGURE 9

Fig. 9. Procedure BIFMCP (Backwards, Interpolate, Forward, Measure, Correlate, Predict) to obtain the site-adapted clearest-sky year CSY_{BIFMCP} for Solar Village.

FIGURE 10

Fig. 10. Procedure MCPI (Measure, Correlate, Predict, Interpolate) to obtain the site-adapted clearest-sky year CSY_{MCPI} for Solar Village.

Figure 11.a shows the CSY_{IMCP} achieved after following the steps described in Figure 8. For its part, Figure 11.b shows 2001, the year of the series with most DNI measurements registered by BSRN. The contrast between both images highlights the virtues of the CSY: a realistic year with the greatest daily energy content, adapted to the site, useful as a testing environment for the characterization of solar equipments.

FIGURE 11

Fig. 11. (a) Site-adapted clearest-sky year CSY_{IMCP} obtained with procedure IMCP (Interpolate, Model, Measure, Correlate, Predict), and (b) DNI measurements of 2001 for Solar Village.

Instead of visualizing the CSY_{BIFMCP} and the CSY_{MCPI}, it is more practical to see the differences between the CSYs. The ideal situation would be to compare with the real DNI measurements corresponding to the moments included in the CSY. However, this is not possible because the radiometer did not work only under clear-sky conditions. In addition, when it measured under clear-sky conditions, the uncertainty inherent to the equipment affected every measurement. So, among these three uncertain series (CSY_{IMCP}, CSY_{BIFMCP} and CSY_{MCPI}), the CSY_{IMCP} has been chosen as the comparison pattern for two reasons. Firstly, models with more inputs tend to be more accurate. Secondly, SMARTS2 has transformed atmospheric variables into DNI measurements to simulate the long-reference series.

Thus, Figures 12 and 13 display in parallel the differences between the CSY_{IMCP} and CSY_{BIFMCP} (CSY_{IMCP} - CSY_{BIFMCP}; Figures 12.a and 13.a), and between CSY_{IMCP} and CSY_{MCPI} (CSY_{IMCP} - CSY_{MCPI}; Figures 12.b and 13.b). Figure 12 depicts the histogram of the relative frequency distribution of the difference (moments with solar altitude under 0º discarded), while Figure 13 exhibits the distribution of the difference along the year.

FIGURE 12

Fig. 12. (a) Relative frequency distribution at Solar Village for CSY_{IMCP} - CSY_{BIFMCP}; (b) Relative frequency distribution at Solar Village for CSY_{IMCP} - CSY_{MCPI} ; (c) Detail of the relative frequency distribution at Solar Village for CSY_{IMCP} - CSY_{BIFMCP} in the range [-1.9 Wm^{-2}, 1.9 Wm^{-2}], and (d) Detail of the relative frequency distribution at Solar Village for CSY_{IMCP} - CSY_{MCPI} in the range [-2 Wm^{-2}, 2 Wm^{-2}]. The CSY_{IMCP} is the site adapted CSY obtained using the IMCP procedure (Interpolate, Model, Measure, Correlate, Predict), CSY_{BIFMCP} with the BIFMCP procedure (Backwards, Interpolate, Forward, Measure, Correlate, Predict), and CSY_{MCPI} with the MCPI procedure (Measure, Correlate, Predict, Interpolate).

FIGURE 13

Fig. 13. Differences distributed throughout the year at Solar Village for (a) CSY_{IMCP} - CSY_{BIFMCP} and (b) CSY_{IMCP} - CSY_{MCPI}. The CSY_{IMCP} is the site-adapted CSY obtained using the IMCP procedure (Interpolate, Model, Measure, Correlate, Predict), CSY_{BIFMCP} with the BIFMCP procedure (Backwards, Interpolate, Forward, Measure, Correlate, Predict), and CSY_{MCPI} with the MCPI procedure (Measure, Correlate, Predict, Interpolate).

It is observed (Fig. 12.a) that in 81.4% (37.2%+44.2%) of the moments with the Sun over the horizon, the IMCP and BIFMCP estimates of the DNI differ by less than ±5 Wm^{-2}. More specifically (see Fig. 12.c), in 52.8% of the moments that difference is less than ±0.1 Wm^{-2}, in 71.2% less than ±1 Wm^{-2}, and in 75% less than ±2 Wm^{-2}. Looking at the rest of the moments with difference over ±5 Wm^{-2}, it is noticeable that the difference is very concentrated around 0, with largest values in the early morning and late afternoon (Fig. 13.a). Though the differences range from -170 Wm^{-2} to 125 Wm^{-2}, these limit values are found to be exceptional. Based on Figure 12.a, the lower and upper bounds are rather -60 Wm^{-2} and 30 Wm^{-2}. For solar concentrating technologies, this discrepancy in the estimates is a minor problem. Normally these technologies do not take advantage of the very first and last moments of the day.

The analogous analysis of differences between IMCP and MCPI is shown in Figures 12.b and 13.b. These differences are larger (range from -240 Wm^{-2} to 520 Wm^{-2}) and spread out throughout the year. In the moments with the Sun over the horizon, 38.4% (8.7%+29.7%) of the IMCP and MCPI estimates of the DNI differ less than ±5 Wm^{-2}. According to Figure 12.d, only 0.7% of all moments have a difference less than ±0.1 Wm^{-2}, 7.8% less than ±1 Wm^{-2}, and 26.4% less than ±2 Wm^{-2}. Figures 12.a and 12.b suggest that the differences between the IMCP and MCPI are more scattered, and spans from -130 Wm^{-2} to 340 Wm^{-2}.

Figures 14.a and 14.b graph the 1-minute mean DNI difference for the entire year for IMCP-BIFMCP and IMCP-MCPI, respectively.

FIGURE 14

Fig. 14. 1-minute mean difference in Solar Village of (a) CSY_{IMCP} - CSY_{BIFMCP}; (b) CSY_{IMCP} - CSY_{MCPI}. The CSY_{IMCP} is the site adapted CSY obtained using the IMCP procedure (Interpolate, Model, Measure, Correlate, Predict), CSY_{BIFMCP} with the BIFMCP procedure (Backwards, Interpolate, Forward, Measure, Correlate, Predict), and CSY_{MCPI} with the MCPI procedure (Measure, Correlate, Predict, Interpolate).

A glance at Figure 14.a reveals that at sunrise and sunset, the BIFMCP clearly overestimates the DNI compared to the IMCP, but behave very similarly in the central hours of the day. The two bumps in the difference are apparently outliers and are only 1.5 Wm^{-2} high each, with a 0.5 Wm^{-2} deep valley in the middle.

Considering Figure 14.b, it can be observed that the MCPI underestimates the DNI, and does so most severely in the early mornings and late afternoons. This can be explained by the fact that MCPI approximates the daily DNI, which is a concave curve, from linear interpolation, since there are no DNI measurements for solar zenith angles higher than 78º. This problem with the differences is intrinsic to the MCPI and can be seen in the list of dates composing the CSY_{MCPI}. Whereas IMCP and BIFMCP chose exactly the same dates to build CSY_{IMCP} and CSY_{BIFMCP}, the MCPI coincided 260 days with the IMCP and BIFMCP, but in the remaining 105 days were for a different date. Another side effect of this same problem of larger differences and MCPI is the annual sum of 1-minute DNI values. The sum of the DNI values in the CSY_{IMCP} is 195.1 MWm^{-2}, for CSY_{BIFMCP} is 195.7 MWm^{-2}, and for CSY_{MCPI} is 189.3 MWm^{-2}. Therefore, the CSY_{BIFMCP} overestimates 0.33% and CSY_{MCPI} underestimates 2.97% with respect to the CSY_{IMCP}.

These results for the MCPI are clearly worse than those attained with the IMCP and BIFMCP, since the process to acquire them is notably simpler. The MCPI propagates data gaps and uses a linear interpolation of the DNI values, instead of filling gaps with the output of good models fed with stable atmospheric parameters that are linearly interpolated, as the other two procedures do. Notwithstanding, it is still worthwhile to consider the MCPI solution. In the hypothetical case of having DNI measurements registered every two minutes, it is very likely that a linear interpolation would be the preferred method to fill the missing data at a 1-minute rate. This approach would gradually lose its appeal as the time step of the measurements increased and the data gap became bigger. So, there exists a tradeoff gap size after which the MCPI is no longer the preferred choice. For Solar Village, the histogram of gaps sizes (Figure 15) shows a majority of 14-minute gaps (usual time step of AERONET), and a substantial quantity of shorter gaps. The represented gaps sizes have intentionally been reduced to those below 60 minutes, but there are still 240 gaps with sizes larger than 60 minutes and, of these, 23 gaps are above 180 minutes. Examining the CSY_{MCPI} day-by-day, there are many satisfactory days. However, these few large gaps significantly penalize the CSY_{MCPI} overall.

FIGURE 15

Fig. 15. Histogram of gaps sizes (deliberately cut at 60 minutes) for the DNI series at Solar Village.

A set of 20 clear-sky days with measurements from BSRN and coincident versions of the CSY_{IMCP}, CSY_{BIFMCP} and CSY_{MCPI} has been selected by visual inspection, in an attempt to evaluate the accuracy of these three CSYs. The coefficients of correlation with that set of 20 days are, for CSY_{IMCP} 0.999629, for CSY_{BIFMCP} 0.999400, and for CSY_{MCPI} 0.998986. This supports the decision of using the CSY_{IMCP} as the reference pattern.

The IMCP and BIFMCP manage large gaps much better than the MCPI. To validate this, the date 16/11/2001, a clear-sky day with all BSRN 1-minute DNI data available, was used. 5 hours of data were artificially removed in the central hours, and the IMCP and BIFMCP were applied as if those data did not exist. The same test was performed in the first hour of the day. Figure 16 displays the results, showing that the IMCP is the method which better fits the measured data.

FIGURE 16

Fig. 16. Performance of the IMCP (Interpolate, Model, Measure, Correlate, Predict) and BIFMCP (Backwards, Interpolate, Forward, Measure, Correlate, Predict) procedures with simulated gaps during the central hours and early morning. (a) Date 16/11/2001 (a clear-sky day with all BSRN 1-minute DNI data available) was used for test purposes. (b) The IMCP and BIFMCP procedures when a 5-hour gap is simulated during the central hours, and the real BSRN data measured during those 5 hours. (c) The IMCP and BIFMCP procedures when a 1-hour gap is simulated in the early morning, and real BSRN data measured during that hour.

As a final point, it remains to deal with the topic of the detection of clear-sky moments to complete a methodology for general purposes. In Solar Village AERONET has been the source to discriminate the clear-sky moments, but normally sites do not have this information on hand. Then, if GHI is known, the algorithm by Lefèvre et al. can be utilized.

Figure 17 reflects the coincidences and discrepancies between the AERONET and Lefèvre's algorithm in the set of clear-sky moments for 2001 declared by AERONET.

FIGURE 17

Fig. 17. From the set of clear-sky moments declared by AERONET for 2001 in Solar Village, (a) shows the clear-sky moments not detected using the Lefèvre's algorithm, and (b) the clear-sky moments detected using the Lefèvre's algorithm. The abscissa axis represents sequentially the 525600 minutes in a year, and every point depicted in the graphs is a clear-sky moment declared by AERONET with its corresponding solar zenith angle in the ordinate axis.

There is good agreement for low solar zenith angles only. Figure 18 quantifies the agreement considering solar zenith angles of 10 degrees.

FIGURE 18

Fig. 18. Agreement in detection of clear-sky moments of Lefèvre's algorithm and AERONET for the data set of clear-sky moments declared by AERONET in the year 2001.

It can be said that in low Sun conditions, AERONET detects better than the Lefèvre's algorithm, although at a cost of promoting 14-minute gaps. The algorithm of Lefèvre et al., however, tends to keep the 1-minute variation of the DNI data, which is important for solar concentrating technologies.

4. CONCLUSIONS

A site-adapted clearest-sky year (CSY) of DNI is a synthetic year composed of the clear-sky days with maximum daily energy content. This CSY sets the theoretical maximum annual radiation for a given site and, therefore, constitutes a pattern useful for tasks of assessing and benchmarking. To generate the CSY, this work developed and validated a methodology of general purpose using three different procedures: IMCP, BIFMCP, and MCPI. The IMCP is the recommended procedure when the atmospheric parameters are available, the BIFMCP should be the chosen method when the DNI measurements are known, and the MCPI is a shortcut of difficult application in practice since the data points should be equally spaced at very short-time steps. For the case of Solar Village, data from the BSRN and AERONET, and the generation of a 1-minute DNI series, there has been shown that the estimates from the IMCP and BIFMCP differ by less than ±5 Wm^{-2} in 81.4% of the moments with the Sun over the horizon, while the estimates of the IMCP and MCPI only agree to this degree at 38.4% of the time. Finally, an algorithm to detect clear-sky moments has shown a good agreement with the clear-sky moments detected by AERONET.

ACKNOWLEDGEMENTS

The authors thank the researchers of AERONET and BSRN for their efforts in establishing and maintaining the Solar Village site, and Gobierno de Navarra for funding the project OptisSolar.

REFERENCES

[1] C.A. Gueymard, Parameterized transmittance model for direct beam and circumsolar spectral irradiance, Sol Energy, 71 (2001) 325-346.

[2] C.A. Gueymard, SMARTS code, version 2.9.5 for Windows. User's manual. Solar Consulting Services, USA. 2005.

[3] R.E. Bird, R.L. Hulstrom, A Simplified Clear Sky Model for Direct and Diffuse Insolation on Horizontal Surfaces. SERI/TR-642-761. Solar Energy Research Institute, Golden, CO, USA. 1981.

[4] C. Rigollier, O. Bauer, L. Wald, On the clear sky model of the ESRA - European Solar Radiation Atlas - With respect to the Heliosat method, Sol Energy, 68 (2000) 33-48.

[5] P. Ineichen, A broadband simplified version of the Solis clear sky model, Sol Energy, 82 (2008) 758-762.

[6] C.A. Gueymard, REST2: High-performance solar radiation model for cloudless-sky irradiance, illuminance, and photosynthetically active radiation - Validation with a benchmark dataset, Sol Energy, 82 (2008) 272-285.

[7] E.L. Maxwell, The solar radiation model used in the production of the National Solar Radiation Data Base (NSRDB), Sol Energy, 62 (1998) 263-279.

[8] National Renewable Energy Laboratory (NREL), National Solar Radiation Data Base. http://rredc.nrel.gov/solar/old_data/nsrdb/, (accessed 31 December 2017).

[9] H.D. Kambezidis, B.E. Psiloglou, D. Karagiannis, U.C. Dumka, D.G. Kaskaoutis, Recent improvements of the Meteorological Radiation Model (MRM) for solar irradiance estimates under all-sky conditions, Ren. Energy 93 (2016) 142-158.

[10] H.D. Kambezidis, B.E. Psiloglou, D. Karagiannis, U.C. Dumka, D.G. Kaskaoutis, Meteorological Radiation Model (MRM v6.1): Improvements in diffuse radiation estimates and a new approach for implementation of cloud products, Ren. Sustain. Energy Rev., 74 (2017) 616-637.

[11] E.L. Maxwell, A quasi-physical model for converting hourly global horizontal to direct normal insolation. SERI/TR-215-3087. Solar Energy Research Institute, Golden, CO, USA. 1987.

[12] R. Perez, P. Ineichen, E.L. Maxwell, R. Seals, A. Zelenka, Dynamic Global-to-Direct Irradiance Conversion Models, ASHRAE Trans., 98 (1992) 354-369.

[13] R. Perez, P. Ineichen, K. Moore, M. Kmiecik, C. Chain, R. George, F. Vignola, A new operational model for satellite-derived irradiances: Description and validation, Sol Energy, 73 (2002) 307-317.

[14] F.X. Kneizys, E.P. Shettle, L.W. Abreu, J.H. Chetwynd, G.P. Anderson, W.O. Gallery, J.E.A. Selby, S.A. Clough, Users Guide to LOWTRAN 7. AFGL-TR- 88-0177. Air Force Geophysics Laboratory, Hanscom AFB, MA, USA. 1988.

[15] A. Berk, L.S. Bernstein, G.P. Anderson, P.K. Acharya, D.C. Robertson, J.H. Chetwynd, S.M. Adler-Golden, MODTRAN cloud and multiple scattering upgrades with application to AVIRIS, Remote Sens Environ, 65 (1998) 367-375.

[16] B. Mayer, A. Kylling, Technical note: The libRadtran software package for radiative transfer calculations - description and examples of use, Atmos Chem Phys, 5 (2005) 1855-1877.

[17] C.A. Gueymard, Direct solar transmittance and irradiance predictions with broadband models. Part I: detailed theoretical performance assessment, Sol Energy, 74 (2003) 355-379.

[18] M. Lefèvre, A. Oumbe, P. Blanc, B. Espinar, B. Gschwind, Z. Qu, L. Wald, M. Schroedter-Homscheidt, C. Hoyer-Klick, A. Arola, A. Benedetti, J.W. Kaiser, J.J. Morcrette, McClear: a new model estimating downwelling solar radiation at ground level in clear-sky conditions, Atmos. Meas. Tech., 6 (2013) 2403-2418

[19] K. Scharmer, J. Reif, The European solar radiation atlas. Vol. 1: Fundamentals and maps, Les Presses de l'École des Mines, Paris, France, 2000.

[20] National Aeronautics and Space Administration (NASA), TOMS-EP. http://science.nasa.gov/missions/toms/, (accessed 31 December 2017).

[21] National Aeronautics and Space Administration (NASA), Terra Science. http://www.nasa.gov/mission_pages/terra/science/index.html, (accessed 31 December 2017).

[22] European Organization for the Exploitation of Meteorological Satellites (EUMETSAT), CM SAF The Satellite Application Facility on Climate Monitoring. http://www.cmsaf.eu/EN/Home/home_node.html, (accessed 31 December 2017).

[23] Meteonorm, Meteonorm: Irradiation data for every place on Earth. http://www.meteonorm.com/, (accessed 31 December 2017).

[24] Solar radiation data (SoDa), SoDa Service - Knowledge in Solar Radiation. http://www.soda-is.com/eng/index.html, (accessed 31 December 2017).

[25] I.J. Hall, R.R. Prairie, H.E. Anderson, Generation of typical meteorological years for 26 SOL-MET stations. SAND 78-1601. Sandia National Laboratories, Albuquerque, NM, USA. 1978.

[26] R. Festa, C.F. Ratto, Proposal of a Numerical Procedure to Select Reference Years, Sol Energy, 50 (1993) 9-17.

[27] M. Gazela, E. Mathioulakis, A new method for typical weather data selection to evaluate long-term performance of solar energy systems, Sol Energy, 70 (2001) 339-348.

[28] D. Thevenard, A. Brunger, The development of typical weather years for international locations: part I, algorithms, ASHRAE Trans., 108 (2002) 376-383.

[29] S. Wilcox, W. Marion, Users manual for TMY3 data sets. TP-581-43156. National Renewable Energy Laboratory, Golden, CO, USA. 2008.

[30] I. García, J.L. Torres, Assessment of the adequacy of EN ISO 15927-4 reference years for photovoltaic systems, Prog. Photovolt: Res. Appl., 23 (2015) 1956-1969.

[31] European Committee for Standardization, EN ISO 15927-4:2005 Hygrothermal performance of buildings -- Calculation and presentation of climatic data -- Part 4: Hourly data for assessing the annual energy use for heating and cooling. International Organization for Standardization (ISO), Geneva, Switzerland, 2005.

[32] P. Narowski, M. Janicki, D.Heim, Comparison of untypical meteorological years (UMY) and their influence on building energy performance simulations. Proceedings of BS2013: 13th Conference of International Building Performance Simulation Association, Chambéry, France. 2013.

[33] D.B. Crawley, L.K. Lawrie, Rethinking the TMY: is the ‘typical’ meteorological year best for building performance simulation? Proceedings of BS2015: 14th Conference of International Building Performance Simulation Association, Hyderabad, India. 2015.

[34] L. Narvarte, E. Lorenzo, Tracking and Ground Cover Ratio, Prog. Photovolt: Res. Appl., 16 (2008), 703–714.

[35] T. Hirsch, H. Schenk, N. Schmidt, R. Meyer, Dynamics of oil-based parabolic trough plants – Impact of transient behaviour on energy yields. Proceedings of the 16th SolarPACES Conference, Perpignan, France. 2010.

[36] C. Thuman, M. Schnitzer, P. Johnson, Quantifying the accuracy of the use of measure-correlate-predict methodology for long-term solar resource estimates, Proceedings of the World Renewable Energy Forum (WREF) 2012, American Solar Energy Society, Denver, CO, USA. 2012.

[37] M. Schnitzer, C. Thuman, P. Johnson, Understanding the variation in estimated long-term solar resource estimates: which data set accurately represents your project site? Proceedings of the World Renewable Energy Forum (WREF) 2012, American Solar Energy Society, Denver, CO, USA. 2012.

[38] M. Šúri, T. Cebecauer, Requirements and standards for bankable DNI data products in CSP projects. Proceedings of SolarPACES 2011 Conference, Granada, Spain. 2011.

[39] C.A. Gueymard, Clear-sky irradiance predictions for solar resource mapping and large-scale applications: Improved validation methodology and detailed performance analysis of 18 broadband radiative models, Sol. Energy, 86 (2012) 2145-2169.

[40] C.A. Gueymard, Aerosol turbidity derivation from broadband irradiance measurements: methodological advances and uncertainty analysis, Proceedings of the American Solar Energy Society Conference, Baltimore, MD, USA. 2013.

[41] J. Remund, L. Wald, M. Lefèvre, T. Ranchin, J. Page, Worldwide Linke turbidity information. Proceedings of the ISES Solar World Congress, International Solar Energy Society, Göteborg, Sweden. 2003.

[42] F. Linke, Transmissions-Koeffizient und Trübungsfaktor, Beitr. Phys. fr. Atmos., 10 (1922) 91-103.

[43] C.N. Long, T.P. Ackerman, Identification of clear skies from broadband pyranometer measurements and calculation of downwelling shortwave cloud effects, J Geophys Res-Atmos, 105 (2000) 15609-15626.

[44] A. Smirnov, B.N. Holben, T.F. Eck, O. Dubovik, I. Slutsker, Cloud-screening and quality control algorithms for the AERONET database, Remote Sens Environ, 73 (2000) 337-349.

[45] J. Polo, L.F. Zarzalejo, P. Salvador, L. Ramírez, Angstrom turbidity and ozone column estimations from spectral solar irradiance in a semi-desertic environment in Spain, Sol. Energy 83 (2009), 257-263.

[46] A. Ohmura, E.G. Dutton, B. Forgan, C. Frohlich, H. Gilgen, H. Hegner, A. Heimo, G. Konig-Langlo, B. McArthur, G. Muller, R. Philipona, R. Pinker, C.H. Whitlock, K. Dehne, M. Wild, Baseline Surface Radiation Network (BSRN/WCRP): New precision radiometry for climate research, B Am Meteorol Soc, 79 (1998) 2115-2136.

[47] B.N. Holben, T.F. Eck, I. Slutsker, D. Tanre, J.P. Buis, A. Setzer, E. Vermote, J.A. Reagan, Y.J. Kaufman, T. Nakajima, F. Lavenu, I. Jankowiak, A. Smirnov, AERONET - A federated instrument network and data archive for aerosol characterization, Remote Sens Environ, 66 (1998) 1-16.

[48] [dataset] G. König-Langlo, A. Bücker, F. Richter, R. Sieger, BSRN snapshot 2014-06 in two ZIP archives (5.63 GB), 2014. doi:10.1594/PANGAEA.833428.

[49] M. Blanco-Muriel, D.C. Alarcón-Padilla, T. López-Moratalla, M. Lara-Coira, Computing the solar vector, Sol Energy, 70 (2001) 431–441.

Figure
Click here to download high resolution image

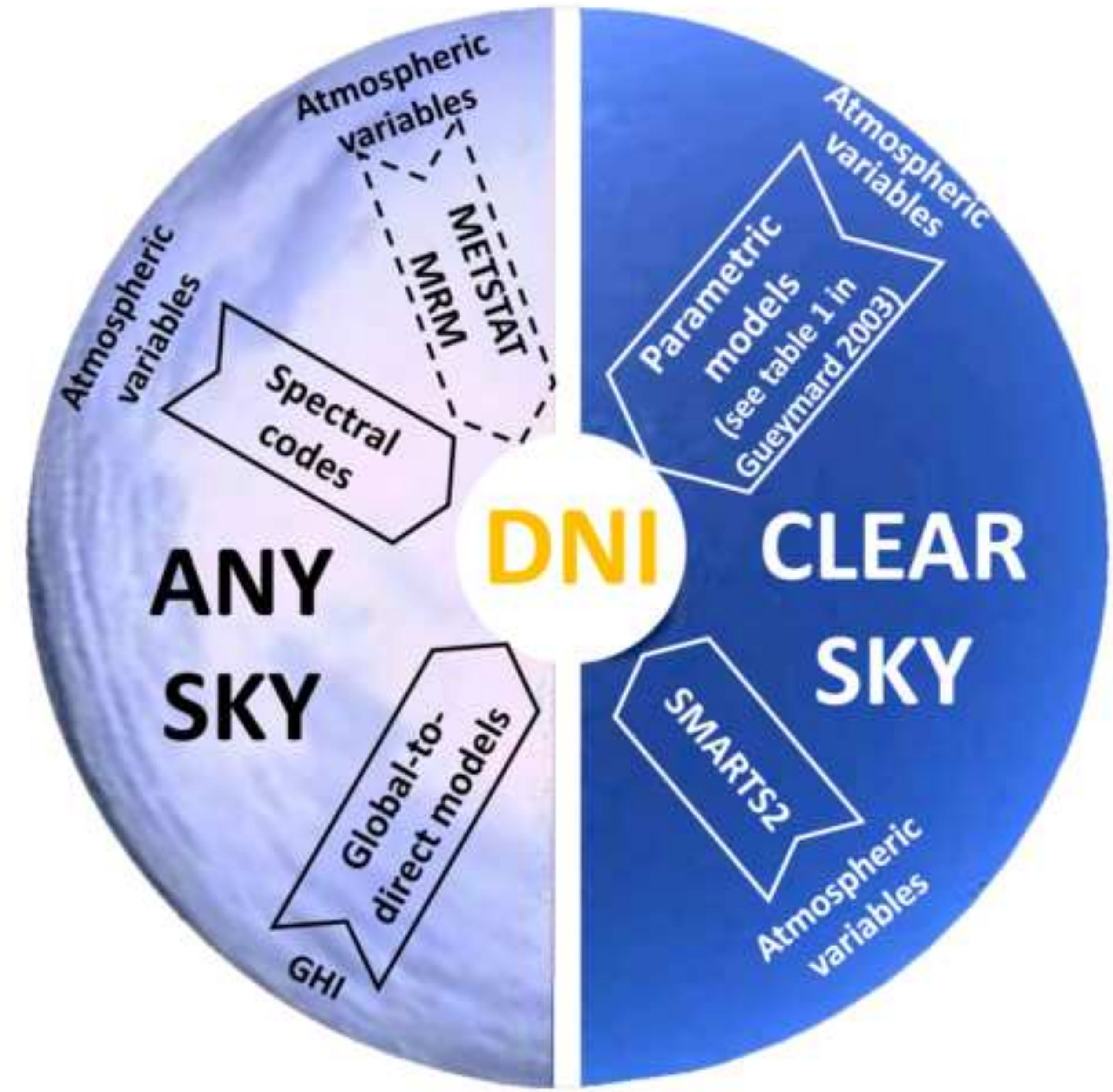

Figure
Click here to download high resolution image

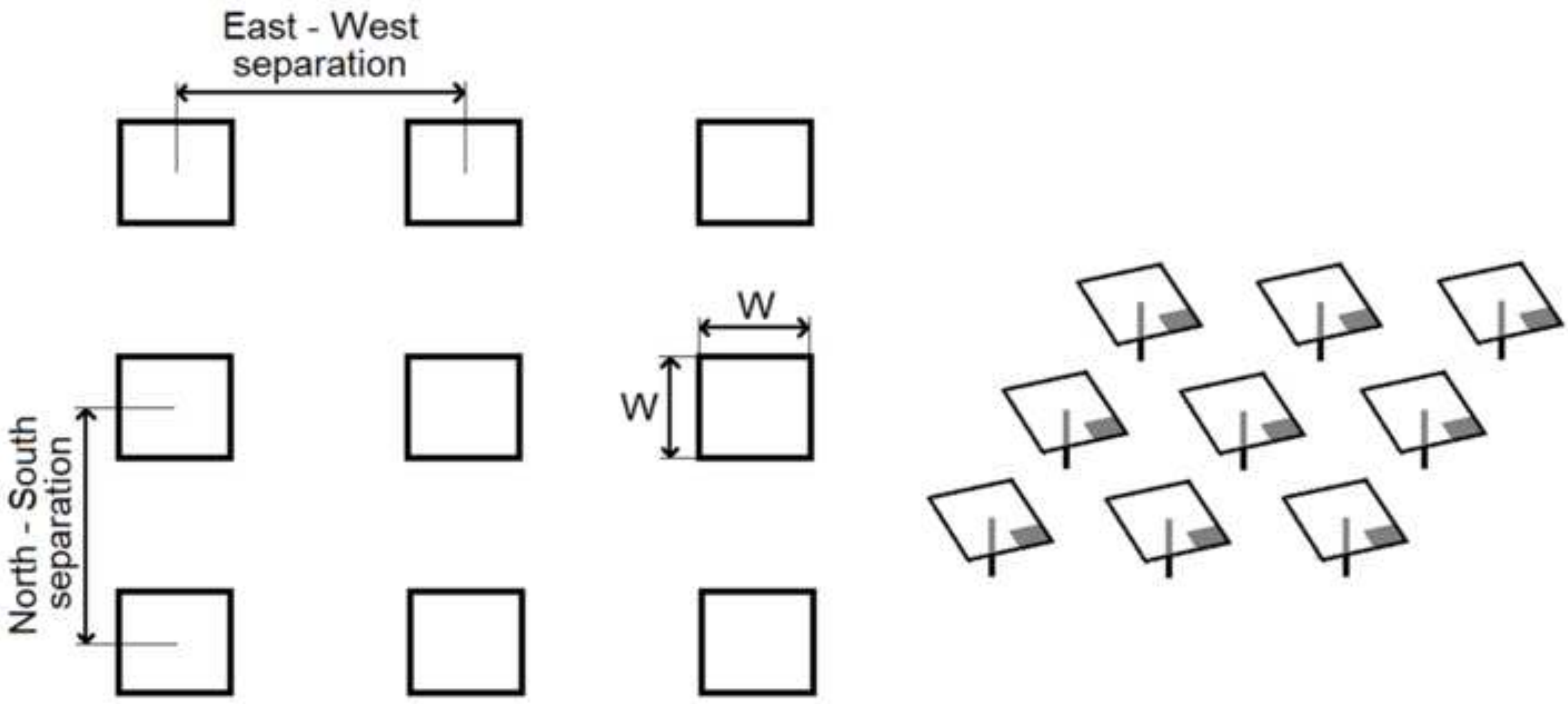

(a)

(b)

Figure
Click here to download high resolution image

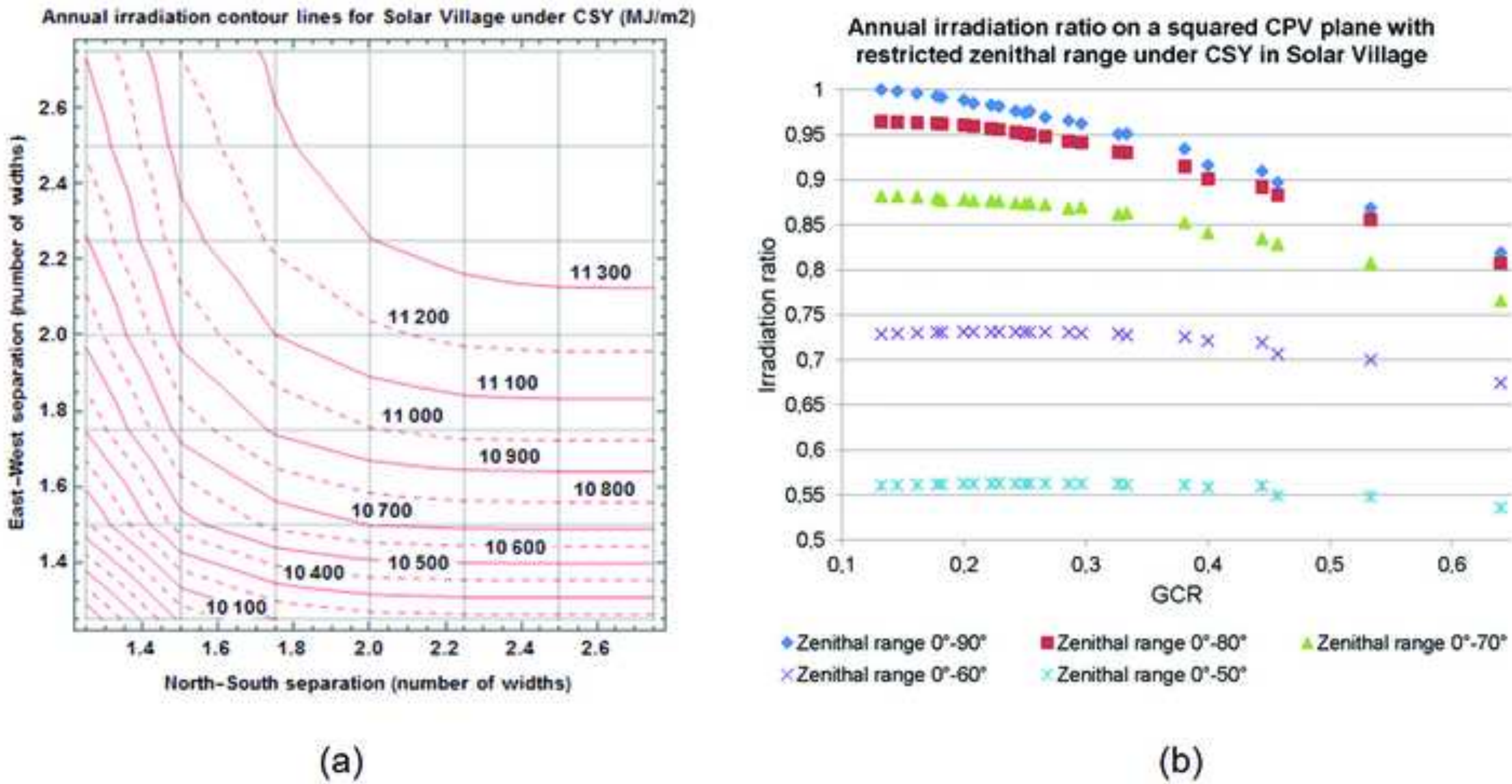

Figure
Click here to download high resolution image

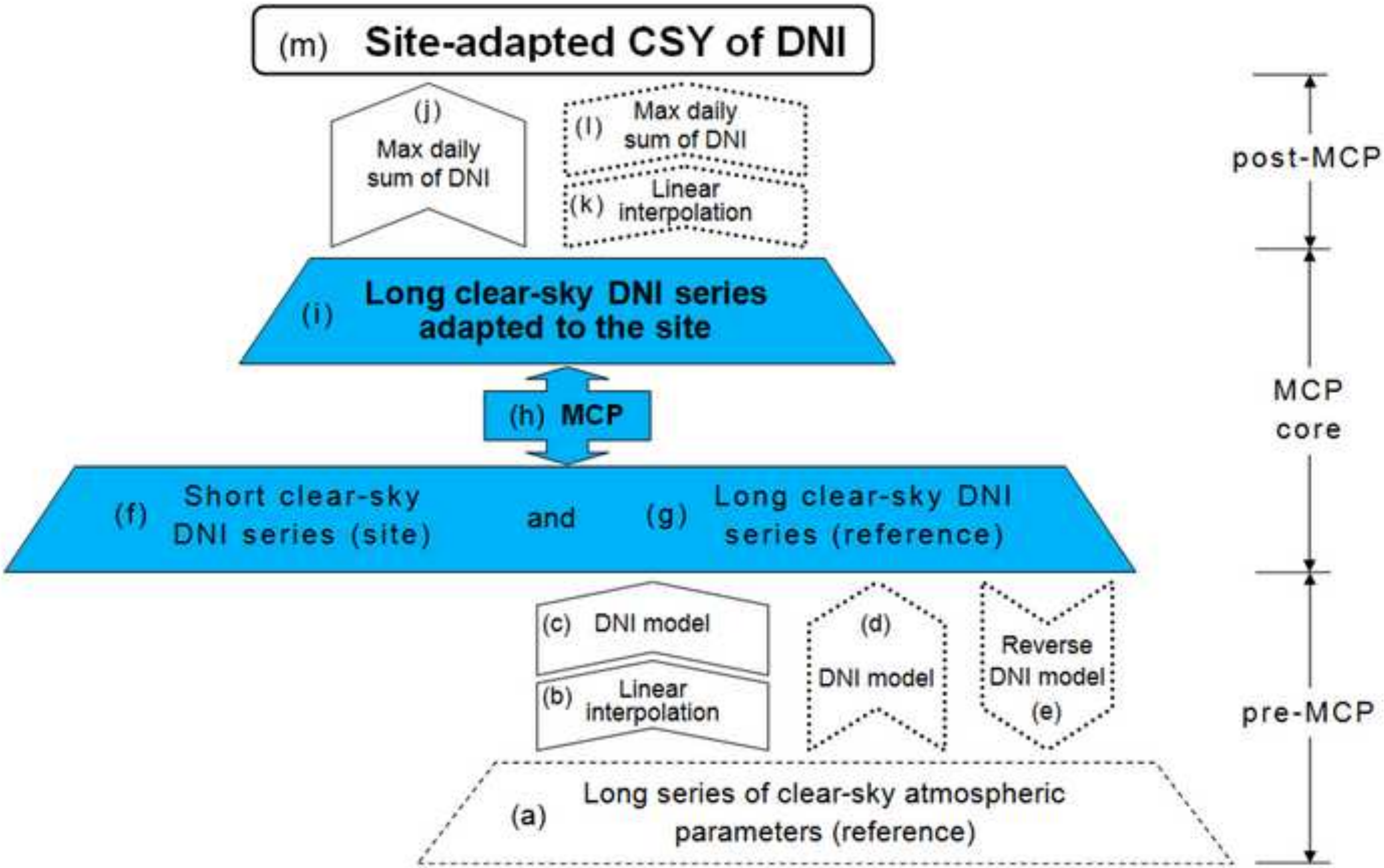

Figure
Click here to download high resolution image

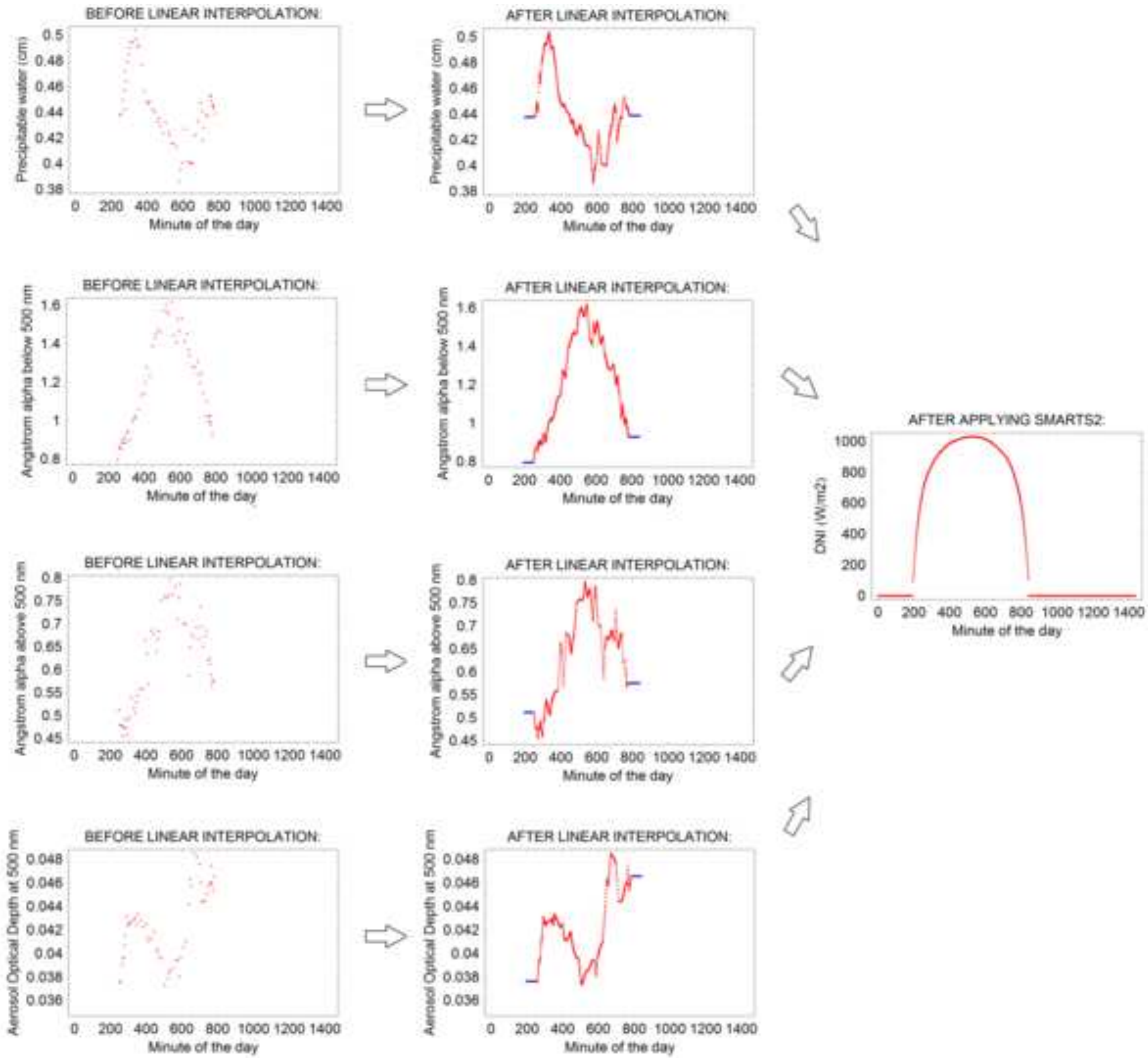

Figure

Click here to download high resolution image

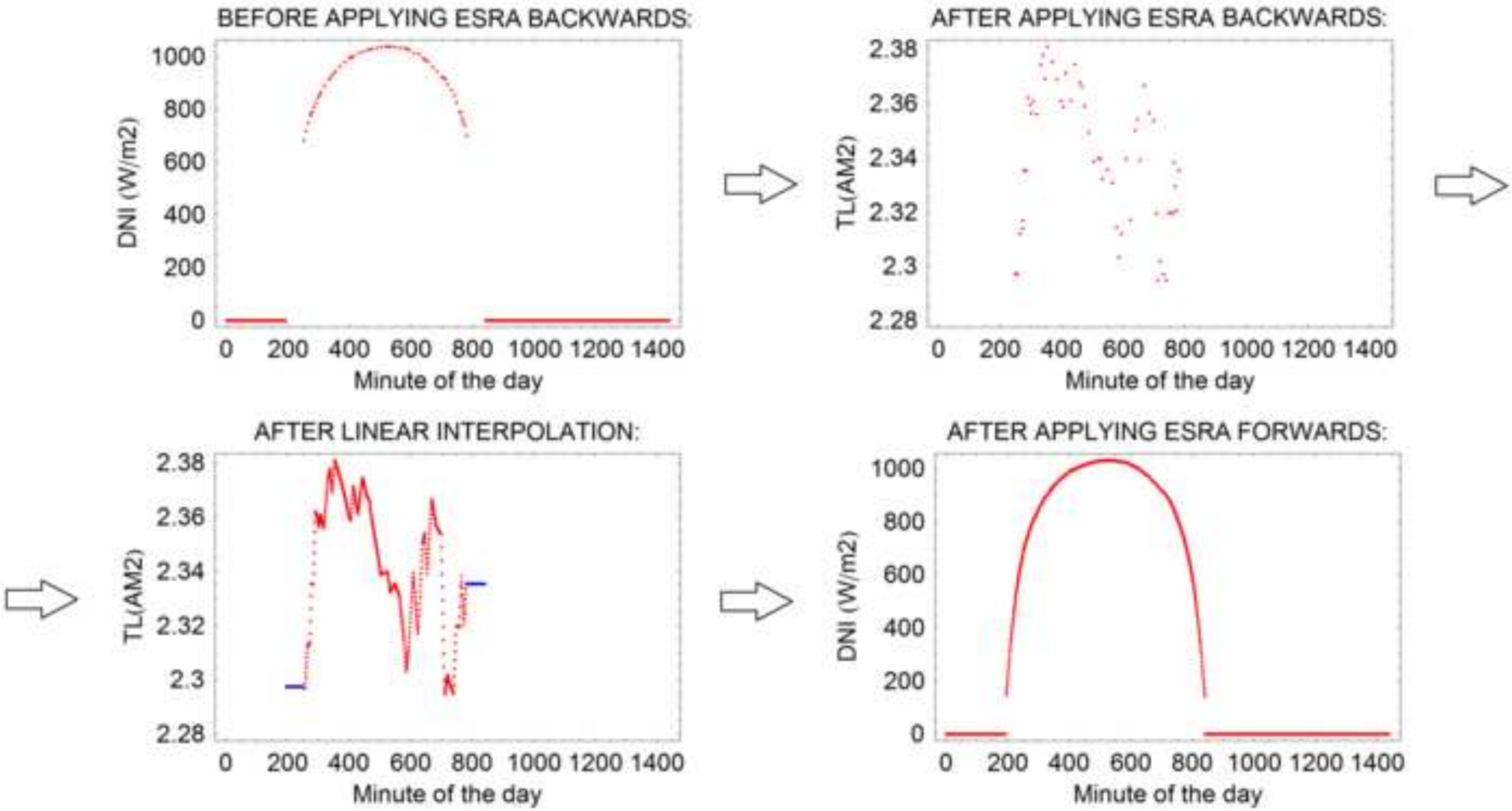

Figure

Click here to download high resolution image

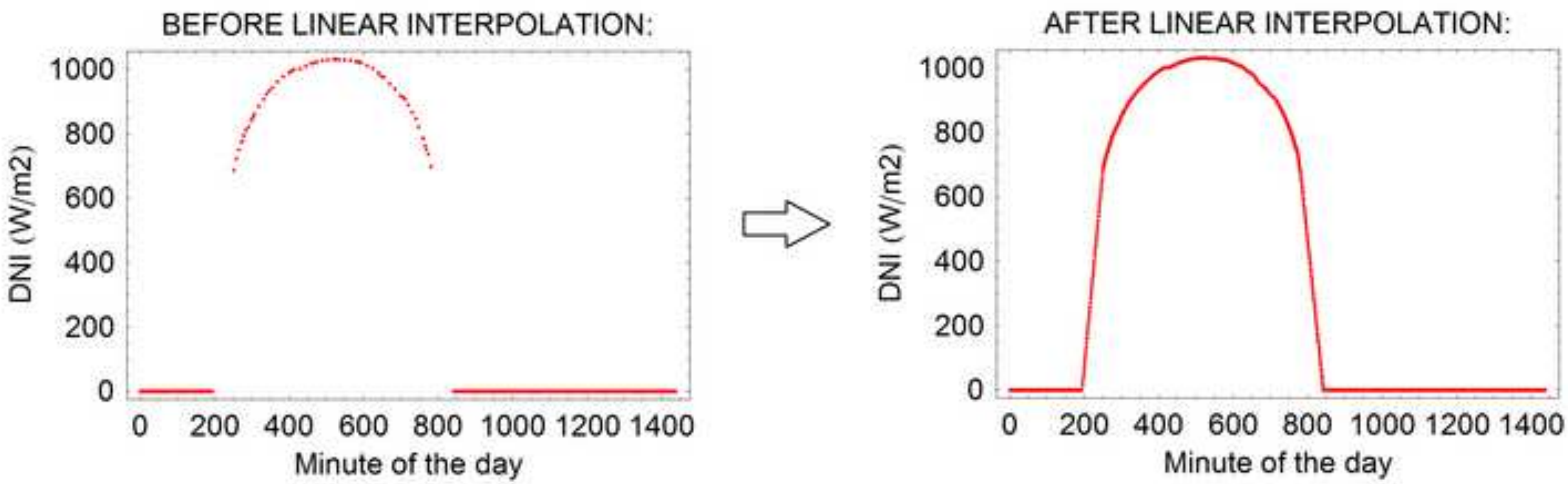

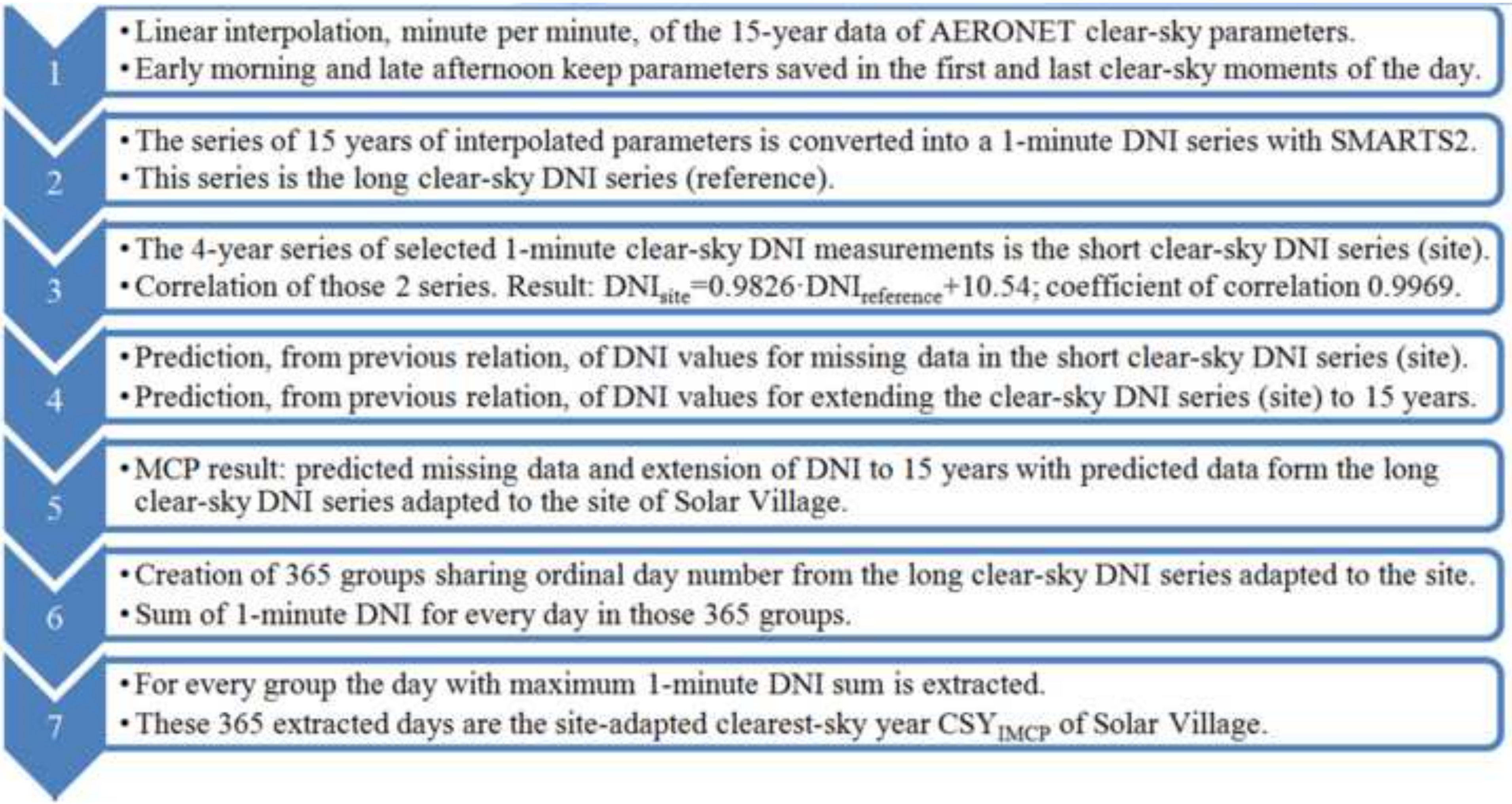
1
• Linear interpolation, minute per minute, of the 15-year data of AERONET clear-sky parameters.
• Early morning and late afternoon keep parameters saved in the first and last clear-sky moments of the day.
2
• The series of 15 years of interpolated parameters is converted into a 1-minute DNI series with SMARTS2.
• This series is the long clear-sky DNI series (reference).
3
• The 4-year series of selected 1-minute clear-sky DNI measurements is the short clear-sky DNI series (site).
• Correlation of those 2 series. Result: $DNI_{site}=0.9826 \cdot DNI_{reference}+10.54$; coefficient of correlation 0.9969.
4
• Prediction, from previous relation, of DNI values for missing data in the short clear-sky DNI series (site).
• Prediction, from previous relation, of DNI values for extending the clear-sky DNI series (site) to 15 years.
5
• MCP result: predicted missing data and extension of DNI to 15 years with predicted data form the long clear-sky DNI series adapted to the site of Solar Village.
6
• Creation of 365 groups sharing ordinal day number from the long clear-sky DNI series adapted to the site.
• Sum of 1-minute DNI for every day in those 365 groups.
7
• For every group the day with maximum 1-minute DNI sum is extracted.
• These 365 extracted days are the site-adapted clearest-sky year CSY_{IMCP} of Solar Village.

Figure

1
- Transformation through SMARTS2 of the 15-year series of AERONET clear-sky parameters to an inferred 15-year DNI series with data gaps. This series is the long clear-sky DNI series (reference).

2
- A series of TL(AM2) from this 15-year DNI series is derived by applying ESRA backwards (eq. 3).

3
- Data gaps in the TL(AM2) series are filled with linear interpolation. Early morning and late afternoon keep TL(AM2) values corresponding to the first and last clear-sky moments registered in the day.

4
- Applying ESRA forwards (eq. 2) converts the TL(AM2) series into a 15-year DNI series without data gaps.
- This series is the long clear-sky DNI series (reference).

5
- The 4-year series of selected 1-minute clear-sky DNI measurements is the short clear-sky DNI series (site).
- Correlation of those 2 series. Result: $DNI_{site}=0.9826 \cdot DNI_{reference}+10.54$; coefficient of correlation 0.9969.

6
- Prediction, from previous relation, of DNI values for missing data in the short clear-sky DNI series (site).
- Prediction, from previous relation, of DNI values for extending the clear-sky DNI series (site) to 15 years.

7
- MCP result: predicted missing data and extension of DNI to 15 years with predicted data form the long clear-sky DNI series adapted to the site of Solar Village.

8
- Creation of 365 groups sharing ordinal day number from the long clear-sky DNI series adapted to the site.
- Sum of 1-minute DNI for every day in those 365 groups.

9
- For every group the day with maximum 1-minute DNI sum is extracted.
- These 365 extracted days are the site-adapted clearest-sky year CSY_{BIFMCP} of Solar Village.

Figure

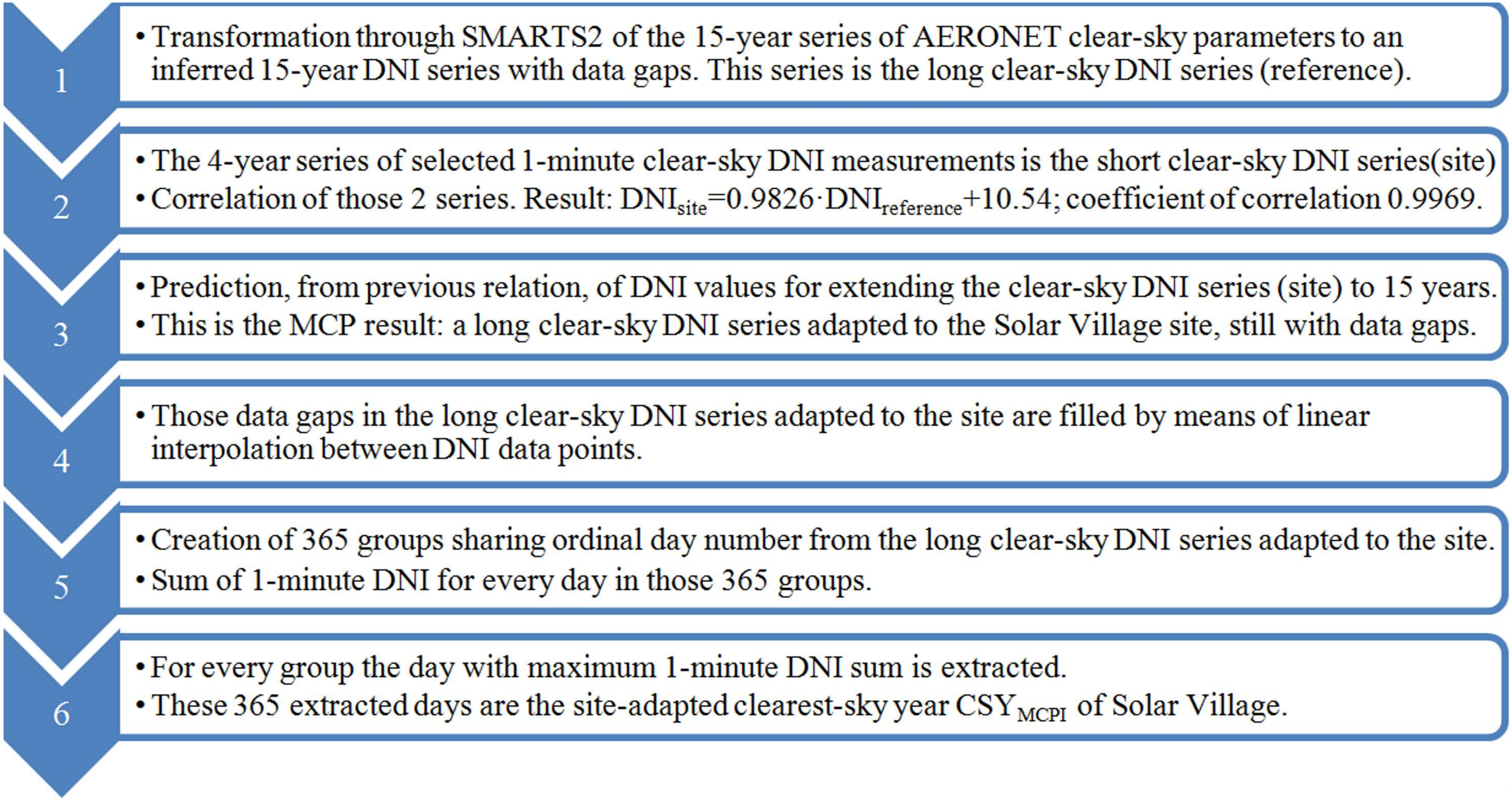
1
• Transformation through SMARTS2 of the 15-year series of AERONET clear-sky parameters to an inferred 15-year DNI series with data gaps. This series is the long clear-sky DNI series (reference).
2
• The 4-year series of selected 1-minute clear-sky DNI measurements is the short clear-sky DNI series(site)
• Correlation of those 2 series. Result: $DNI_{site}=0.9826 \cdot DNI_{reference}+10.54$; coefficient of correlation 0.9969.
3
• Prediction, from previous relation, of DNI values for extending the clear-sky DNI series (site) to 15 years.
• This is the MCP result: a long clear-sky DNI series adapted to the Solar Village site, still with data gaps.
4
• Those data gaps in the long clear-sky DNI series adapted to the site are filled by means of linear interpolation between DNI data points.
5
• Creation of 365 groups sharing ordinal day number from the long clear-sky DNI series adapted to the site.
• Sum of 1-minute DNI for every day in those 365 groups.
6
• For every group the day with maximum 1-minute DNI sum is extracted.
• These 365 extracted days are the site-adapted clearest-sky year CSY_{MCPI} of Solar Village.

Figure
Click here to download high resolution image

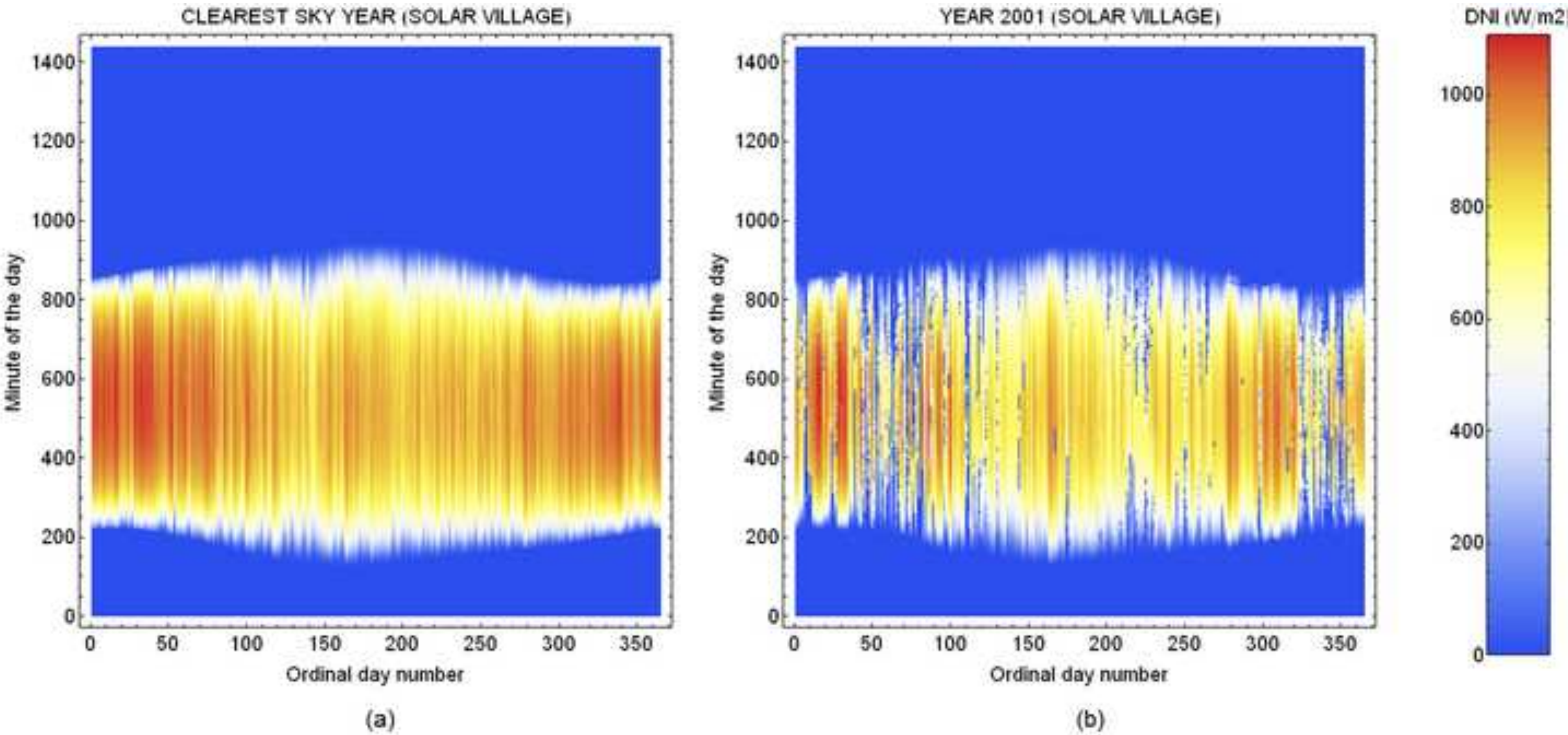

Figure

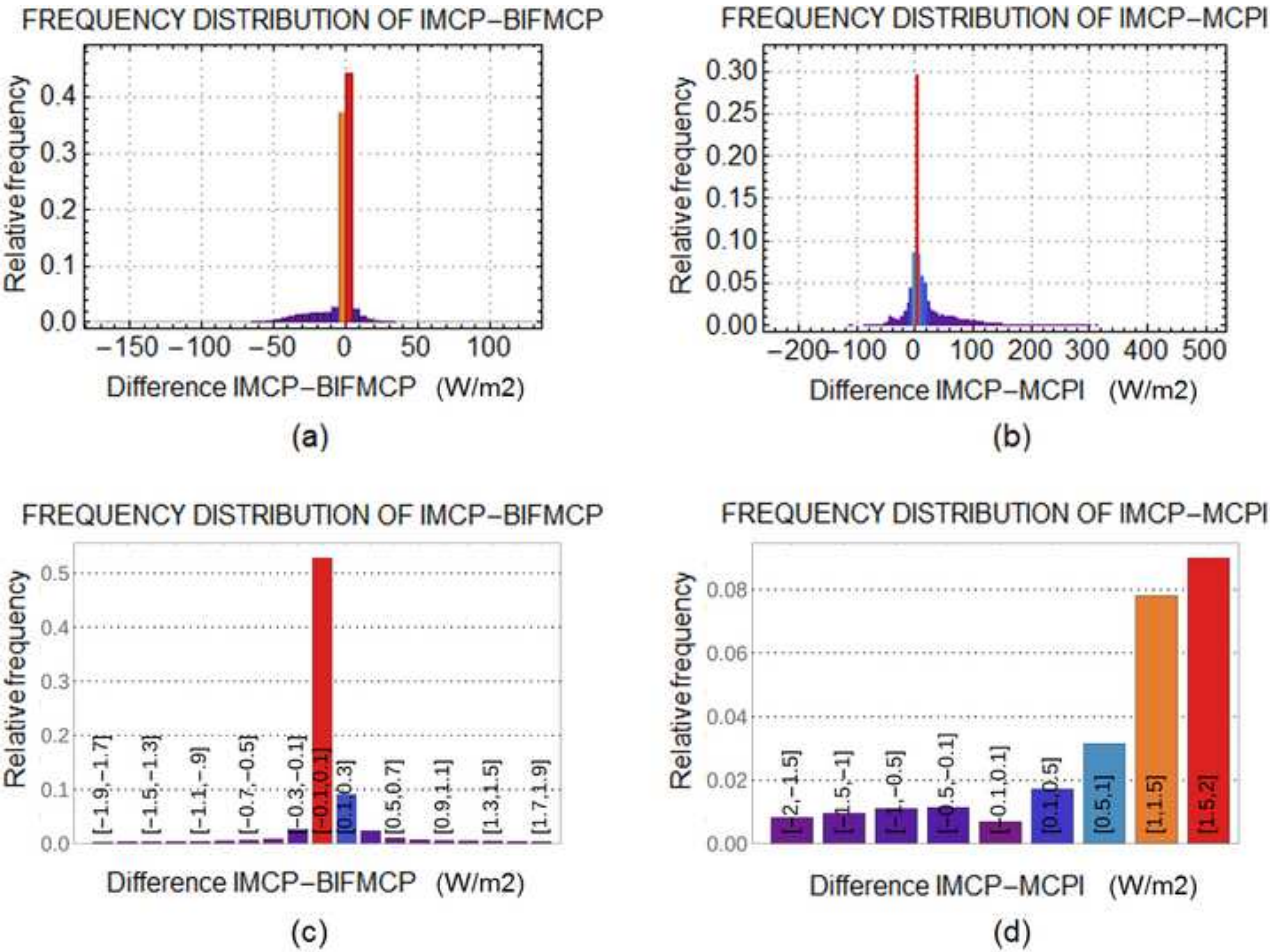

FREQUENCY DISTRIBUTION OF IMCP−BIFMCP
Relative frequency
0.0
0.1
0.2
0.3
0.4
−150
−100
−50
0
50
100
Difference IMCP−BIFMCP (W/m2)
(a)
FREQUENCY DISTRIBUTION OF IMCP−MCPI
Relative frequency
0.00
0.05
0.10
0.15
0.20
0.25
0.30
−200
−100
0
100
200
300
400
500
Difference IMCP−MCPI (W/m2)
(b)
FREQUENCY DISTRIBUTION OF IMCP−BIFMCP
Relative frequency
0.0
0.1
0.2
0.3
0.4
0.5
[−1.9,−1.7]
[−1.5,−1.3]
[−1.1,−.9]
[−0.7,−0.5]
[−0.3,−0.1]
[−0.1,0.1]
[0.1,0.3]
[0.5,0.7]
[0.9,1.1]
[1.3,1.5]
[1.7,1.9]
Difference IMCP−BIFMCP (W/m2)
(c)
FREQUENCY DISTRIBUTION OF IMCP−MCPI
Relative frequency
0.00
0.02
0.04
0.06
0.08
[−2,−1.5]
[−1.5,−1]
[−1,−0.5]
[−0.5,−0.1]
[−0.1,0.1]
[0.1,0.5]
[0.5,1]
[1,1.5]
[1.5,2]
Difference IMCP−MCPI (W/m2)
(d)

Figure
Click here to download high resolution image

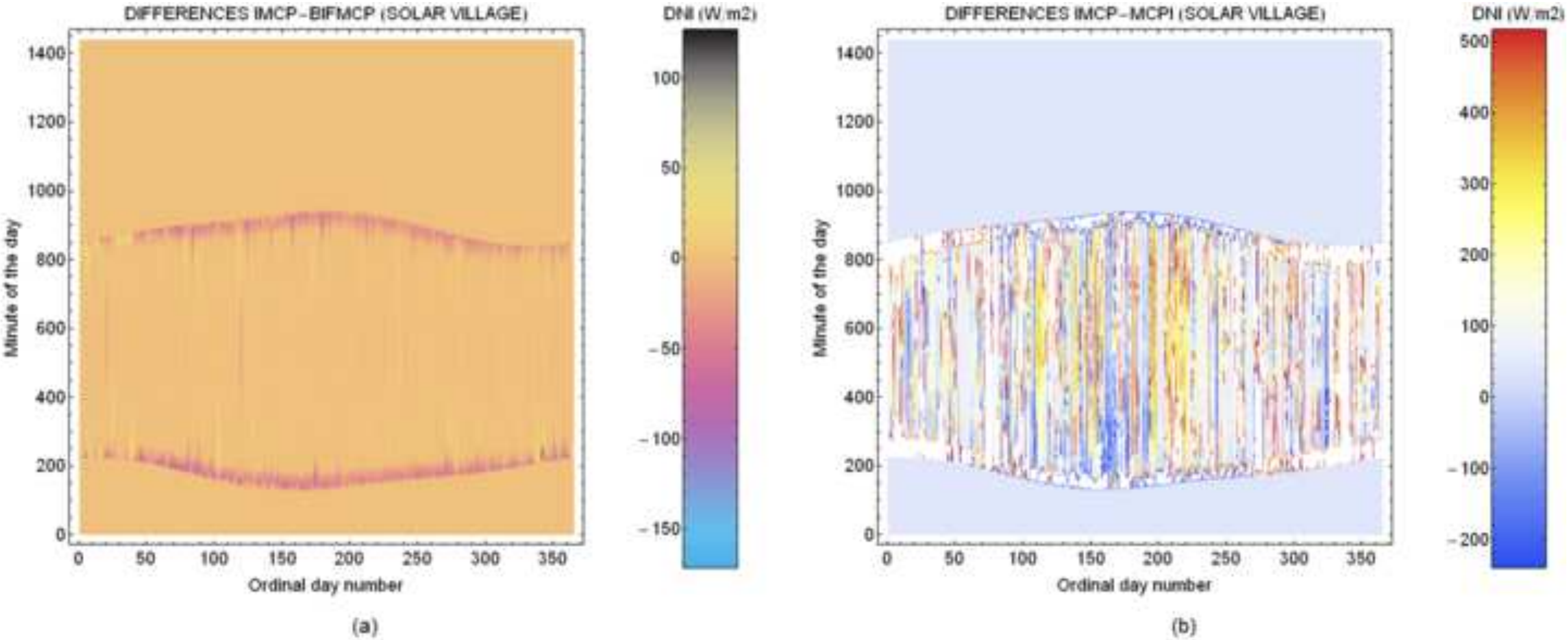

Figure

Click here to download high resolution image

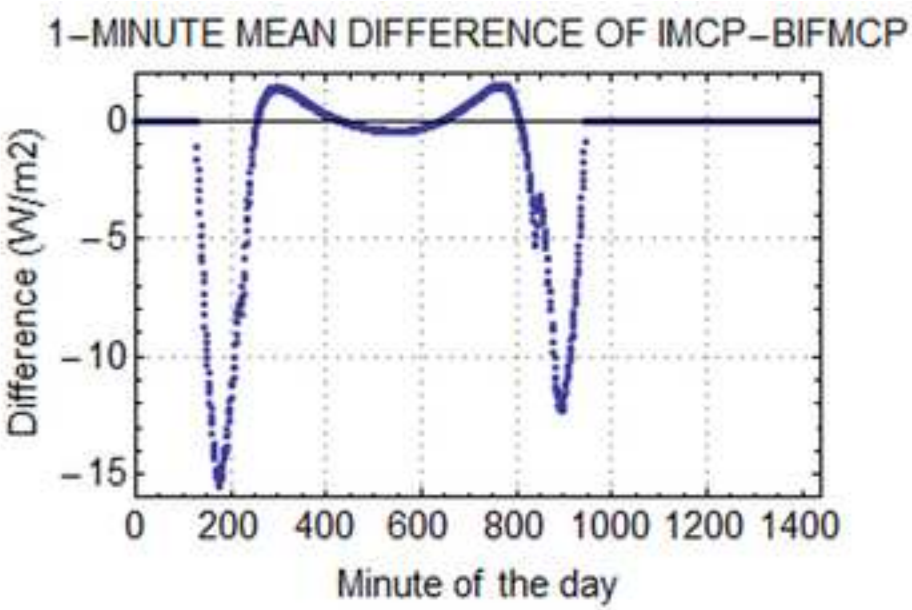

(a)

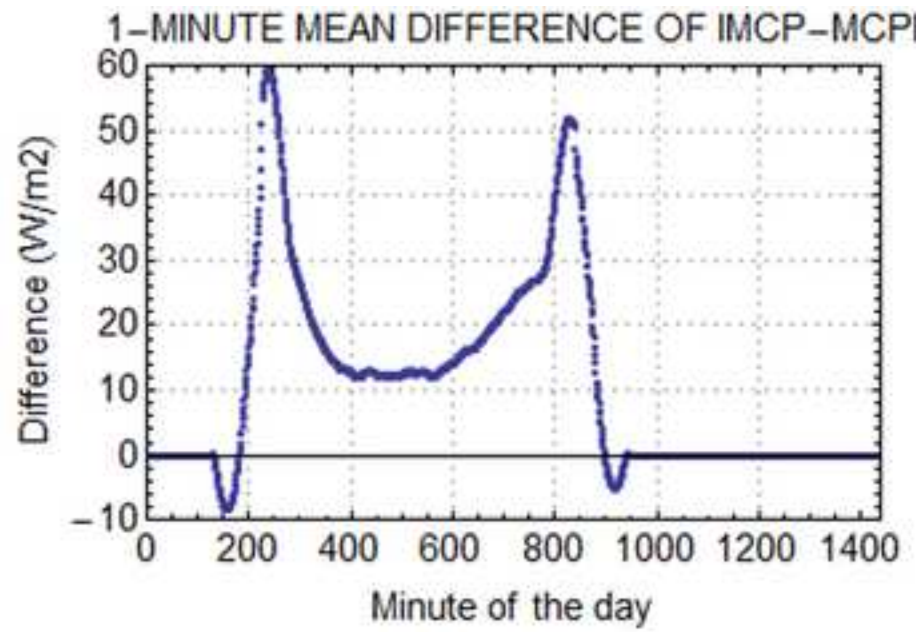

(b)

Figure
Click here to download high resolution image

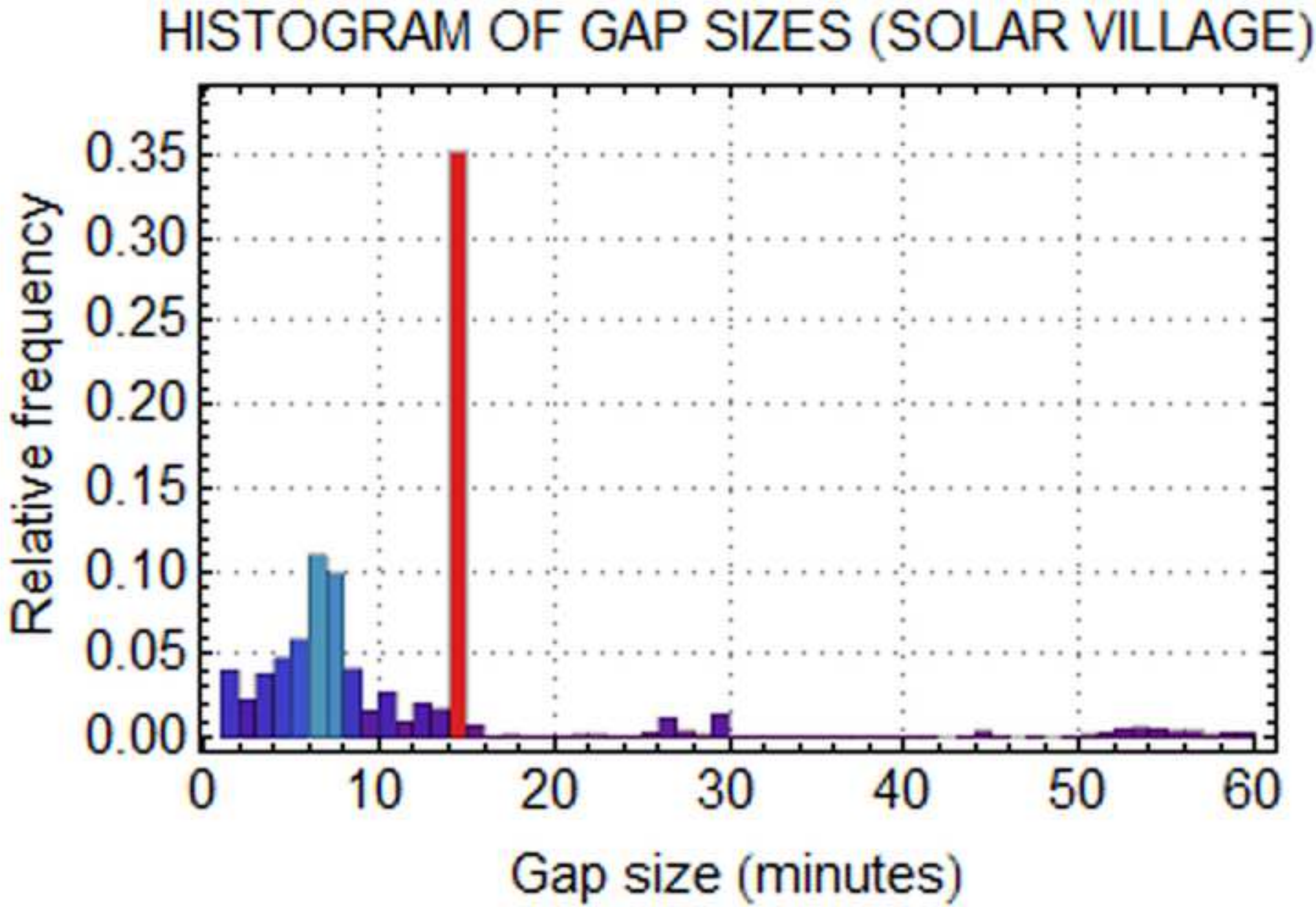

Figure
Click here to download high resolution image

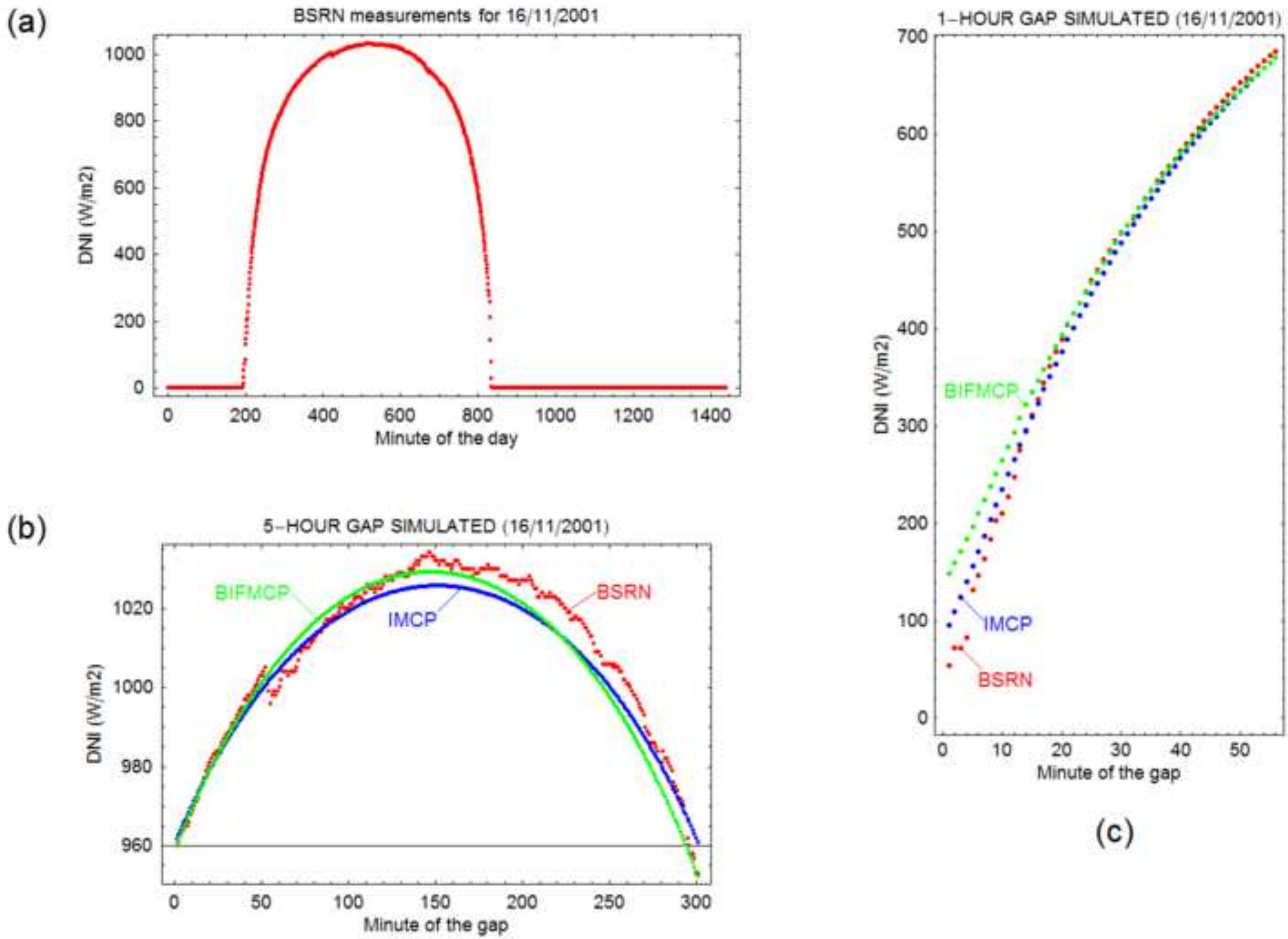

Figure
Click here to download high resolution image

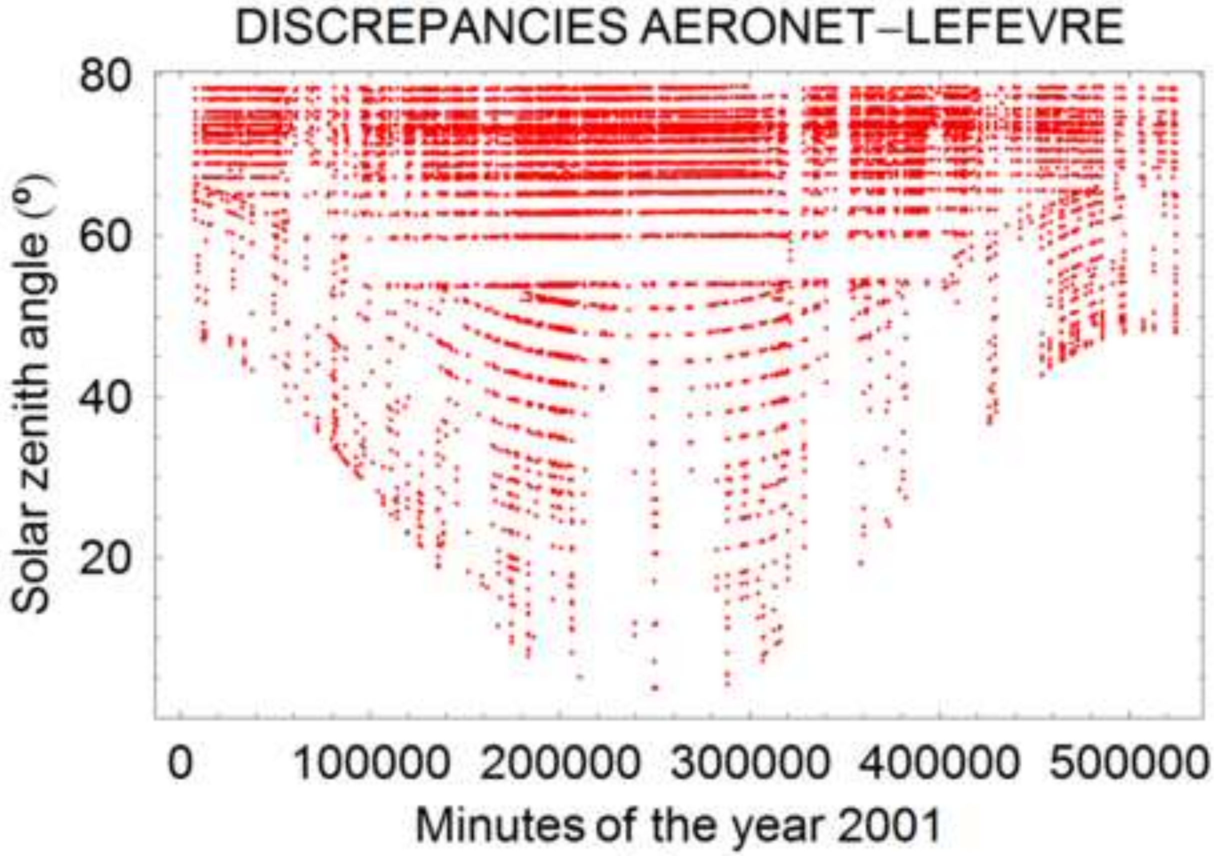

(a)

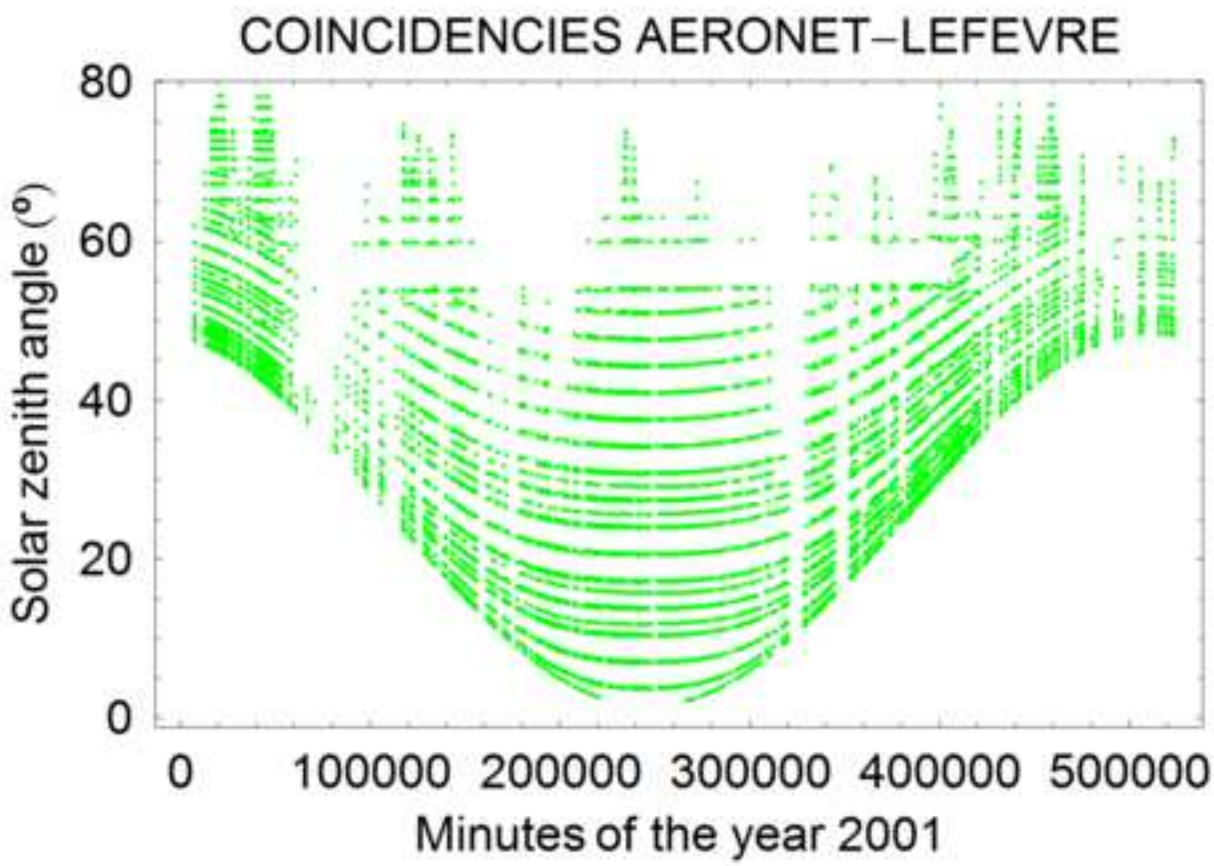

(b)

Figure
Click here to download high resolution image